University of Stavanger

FACULTY OF SCIENCE AND TECHNOLOGY

MASTER'S THESIS

Study programme/specialisation: Petroleum Engineering/ Natural gas Technology	Spring/ ~~Autumn semester~~, 2020.. Open / ~~Confidential~~
Author: Erfan Abolghasemi	
Programme coordinator: Anita Malde Rasmussen Supervisor(s): Pål Østebø Andersen, Dhruvit Satishchandra Berawala	
Title of master's thesis: Influence of Adsorption Layer Thickness in Tight Compressible Shales subject to Gas Production	
Credits: 30	
Keywords: Adsorption model, Adsorbed layer thickness, Compressible shale, Shale gas production	Number of pages: 66…… + supplemental material/other: …… Stavanger, ..15/07/2020….. date/year

Abstract

The gas transport in shale nanopores has always been a major concern in developing shale gas reservoirs. Different gas flow regimes in shale nanopores have been studied and classified during recent years. Some mathematical models have been driven to explain and simulate how shale gas reservoir performance works during gas production. In tight shales, gas is stored in both free and adsorbed forms, where the latter can make a significant part of the gas in place.

In this work, we implement an adsorption model where the adsorbed layer thickness is a function of pore geometry and dimension, total pressure, and free gas saturation. The shale is assumed to be compressible, and its porosity and pore radius may reduce because of pressure depletion. The effective pore radius, which also depends on adsorption layer thickness, is assumed to control permeability. We investigate the impact of varying adsorbed layer thickness on porosity, permeability, and overall gas recovery. Higher Recovery of shale gas is observed when we consider varying adsorption thickness compared to constant adsorption thickness. Changes in permeability due to pore geometry and dimensions show distinctly different behavior during the desorption of gas. Through a series of simulations, the most critical parameters of the system are identified.

It is concluded that the adsorbed layer thickness and compressibility of the shale matrix play an important role and should be considered in evaluating the efficiency of shale gas recovery. Overall, this work provides an intuitive modeling approach to identify the ideal scenarios for shale gas production.

Keywords: Adsorption model, Adsorbed layer thickness, Compressible shale, Shale gas production

Acknowledgements

Apart from the efforts of myself, the success of any project depends largely on the encouragement and supports of many others. I take this opportunity to express my gratitude to the people who have been instrumental in the successful completion of this project. I would like to show my greatest appreciation to **Pål Østebø Andersen** (Department of Energy Resources, University of Stavanger). I can't say thank you enough for his tremendous support and help. I feel motivated and encouraged every time I attend his meeting. Without his encouragement and guidance this project would not have materialized. Also I would like to extend my sincere thanks to **Dhruvit Satishchandra Berawala** (Department of Energy & Petroleum Engineering, University of Stavanger). The guidance and support received from him, was vital for the success of the project. I am grateful for their constant support and help.

I would like to thank my parents & my partner, who have supported me throughout entire process, both by keeping me harmonious and helping me putting pieces together. I will be grateful forever for your love.

Table of Content

List of Figures

List of Tables

Nomenclature

â	=	Adsorbed component, Pa
A	=	surface area, m^2
A_p	=	surface area of the pore, m^2
A_s	=	surface area of the solid, m^2
C	=	Constant conversion factor, dimensionless
C_g	=	Adsorbed gas to shale, m^3/ kg
C_{max}	=	Maximum amount of gas that can be adsorbed to shale, m^3/ kg
C_k	=	organic matter total compressibility, Pa^{-1}
C_a		Langmuir volume on the organic matter surface, mol / m^3
f_c	=	Knudsen's correction factor
$GCIP$	=	Gas currently in place, Pa
k	=	Absolute Darcy permeability, m^2
K_a	=	Apparent permeability, m^2
k_∞	=	liquid permeability of porous media, m^2
K_n	=	Knudsen number, dimensionless
L	=	System length, m
M	=	Molecular weight, kg / mol
M_1	=	Mass of free gas in the matrix, Pa
M_2	=	Mass of adsorbed gas in the matrix, Pa
N	=	total Number of pores per bulk volume, dimensionless
$OGIP$	=	Original gas in place, Pa
p	=	pressure of the free gas, Pa
p_L	=	Langmuir pressure, Pa
p_{ini}	=	Initial pressure of the shale gas reservoir, Pa
p_o	=	Pressure in organic matter, Pa
q	=	Gas flow, m^3/ s
R_0		Original Pore radius, m
R	=	Current Pore radius, m

$R_{effective}$	=	Effective Pore radius, m
ΔR	=	Adsorption thickness, m
R_g	=	Gas constant, J/ K mol
R_h	=	hydraulic radius, m
RF	=	Recovery factor, dimensionless
RF_∞	=	Ultimate recovery factor, dimensionless
RF_{frac}	=	Fraction of ultimate recovery factor, dimensionless
S_g	=	Saturation of free gas, mol / m^2
S_a	=	Saturation of adsorbed gas, mol / m^2
T	=	Absolute temperature, K
u	=	Gas velocity, m/s
V_n	=	Volume of n-sphere pore, m^3
V_n^0		Volume of n-sphere pore at initial time, m^3
V_p	=	Pore volume, m^3
V_s	=	Solid volume, m^3
V_f	=	Volume of free gas, m^3
V_a	=	Volume of adsorbed gas, m^3
Z	=	Real gas deviation factor, dimensionless
α_K	=	Rarefraction parameter, dimensionless
μ	=	Gas viscosity, Pa s
ρ_g	=	Free gas density, kg / m3
ρ_a	=	Adsorbed gas density, kg / m3
ρ_{av}	=	Average density, kg / m3
τ	=	Tortuosity, dimensionless
ϕ	=	Porosity, dimensionless
ϕ_0	=	Porosity at initial time, dimensionless
ϕ_{app}	=	Apparent porosity, dimensionless
Γ	=	Gamma function

ε_{ks}	=	The proportion of solid matrix volume in the total interconnected matrix pore volume
λ	=	Mean-free-path of molecules, m

1. Introduction

Shale revolution has been an important topic during recent years. The shale story started in 2006 from the Haynesville shale in East Texas, United state initially focusing on natural gas, and then it shifted to crude oil in following years (Blum 2019). The interest in assessing the shale gas resources in the world is increasing drastically. Therefore, many companies have intensified their exploration efforts to establish the presence and volume of prospective natural gas resources (Weijermars 2013).

Using engineering skills, companies can recover the massive amount of inaccessible natural gas trapped in shale reservoirs. However, this means that drilling engineers had to turn their instruments from vertical to horizontal (Kerr 2010). Horizontal drilling and hydraulic fracturing have been used to develop shale gas fields due to extremely low permeability of shale (Yuan, Deng et al. 2013). Hydraulic fracturing, or sometimes called fracing in rocks, takes place when the fluid pressure in the rock exceeds the smallest principal stress plus the tensile strength of the rock. This results in making fractures in the rock. In shale reservoirs, artificial or human-made hydraulic fracturing occurs, which is generally done by increasing the borehole's fluid pressure. This increase in pressure will result in splitting and fracturing in the direction of the least resistance. Hydraulic fracturing has been used commercially as a stimulation technique in reservoirs with low permeability since the early fifties (Fjar, Holt et al. 2008).

Hydraulic fracing involves various surface and subsurface risks, among these major risks, are the use of fracturing fluids that contain toxins; groundwater and surface water contamination due to migration of hydrocarbons, heavy metals, and radioactive substances from nearby formations; extreme consumption of water for fracturing; air emissions; sedimentation; earthquakes; explosion; and human health effects. These hazards need to be assessed and minimized. Environmental concerns over traditional hydraulic fracturing using a mixture of water, sand, and small amounts of chemicals made scientists look for more environmentally friendly techniques like CO2 injection (Rivard, Lavoie et al. 2014, Loh and Loh 2016).

The other reason that makes engineers think about injecting CO2 is that the estimated ultimate recovery (EUR) is really poor during the early stages of field development in shale reservoirs (Weijermars 2013). It is stated that only 3-10 % of gas can be economically recovered through natural depletion from tight shale (Berawala and Østebø Andersen 2019). As a result, interest in enhanced shale gas recovery (ESGR) has grown in recent years (Kim, Cho et al. 2017). For acquiring the sufficient knowledge about shale gas and perform enhance shale gas recovery (ESGR), it is important to fully understand the microscopic properties of gas in the shale (Ghanbari and Dehghanpour 2015).

Unconventional gas reservoirs are known by complex geological and petrophysical systems, just like conventional reservoirs. There are also heterogeneities at all scales in unconventional gas reservoirs. The difference for unconventional gas reservoirs, however, is the unique gas storage and producing characteristics. As a result, a realistic description is needed to quantify the range and value of gas-in-place. Precise characterizations are also needed to identify the reservoir mechanisms which affect the production and final recovery (Newsham and Rushing 2001).

Shale gas reservoirs normally have a net thickness of 50 to 600 ft, porosity of 2-10%, total organic carbon (TOC) of 1-14% and are found at depths of 1000 to 13000 ft (Cipolla, Lolon et al. 2010). Shale is known to be a very fine-grained and clastic sedimentary rock, the pore structures of shale

is very complex, permeability is extremely low and it has high clay content (Shen, Xu et al. 2016, Shen, Li et al. 2017). The heterogeneity of pore structure in shale gas reservoirs is another characteristic of this formation. Organic matter, nonorganic matrix, natural fractures and pore space resulted by hydraulic fractures are among this heterogeneity which organic matter is the main part of a productive shale gas reservoir. (Javadpour, Fisher et al. 2007, Bustin, Bustin et al. 2008). All these variation of pores scales results in complexity of gas flow in shale gas reservoirs. Another difficulty that is concern with shale reservoirs is the challenge to evaluate them using conventional laboratory techniques. This is due to the fact that core samples are often subjected to stress release fractures, which results in over measurement of rock properties (Javadpour, Fisher et al. 2007).

There are two forms of gas in shale gas reservoirs. The first form is the adsorbed gas, which exists on organic matter and inorganic mineral surfaces, and the second form is compressed gas or so-called free gas in fractures and pore voids (Shen, Li et al. 2017). The available area for gas adsorption is defined by pore-size distribution and surface area of organic and mineral fractions in shale (Strapoc, Mastalerz et al. 2010). The micro-porous organic matter structure provides a massive total surface area to sorb the gas (Chalmers and Bustin 2007). It is not entirely clear that what is the role of mineral matter in shale gas adsorption, yet, the relationship between organic matter and gas sorption can be affected by mineral matter (Ross and Bustin 2009).

Over the past years, many transport models have been created to evaluate and quantify the flow of gas in shale gas reservoirs. Some of these studies proposed a model for transportation of gas in shales, which includes viscous flow and Knudsen flow. Other studies considered four regimes to present a thorough review of flow models in shale gas reservoirs (Moridis, Blasingame et al. 2010, Freeman, Moridis et al. 2011). Clarkson et al introduced a dynamic-slippage model to study the production dynamics in shale gas reservoirs (Clarkson, Nobakht et al. 2012). Knudsen diffusion was extended into slippage factor by other researchers to explain gas transportation in shale gas reservoirs (Civan, Rai et al. 2011). Also, an experimental model has been proposed by Anderson et al. to describe the transport mechanisms (Anderson, Moorman et al. 2014).

Although many models are introduced to explain gas transportation in shale reservoirs, a detailed comparison and flow patterns analysis is lacking. Moreover, many different parameters on gas flow patterns, such as pressure, compressibility, and adsorption parameters, such as adsorption layer thickness, are not studied systematically. Therefore, it is crucial to understand gas flow behavior in shale reservoirs and its effects on different flow patterns. This will bring the opportunity to predict gas production better and optimize the fracturing process for shale gas reservoirs.

In this work, the gas flow in shale reservoirs is described by using Knudsen number. The gas flow mathematical model is derived and proposed by considering the effect of different gas flow parameters such as porosity, apparent permeability, adsorption layer thickness, free gas saturation, pore geometry, and dimension. Results of the study on each property as a function of pressure are analyzed. Besides, a series of dynamic simulations are studied to quantify these parameters. The influence of adsorption, adsorption thickness, compressibility, and pore geometry on the gas flow behavior is performed. Changes in reservoir properties due to pore geometry and dimensions are also investigated.

With the objective of investigating the effect of pore geometry's dimension, adsorbed layer thickness, and compressibility, this work should provide insights for a better understanding of gas flow behavior in shale nanopores.

2. Mathematical Model

2.1. Geometry and variables

Consider a gas production from a shale matrix system (e.g. a core sample) with length L, see **Figure 1** and a no-flow boundary on the right side of the core. Inside this shale matrix we assume pores with shape of an n-sphere. This means for n=1 it is a fracture, for n=2 a cylinder and for n=3 a sphere. We only consider methane (single-phase and single component) to simplify the problem.

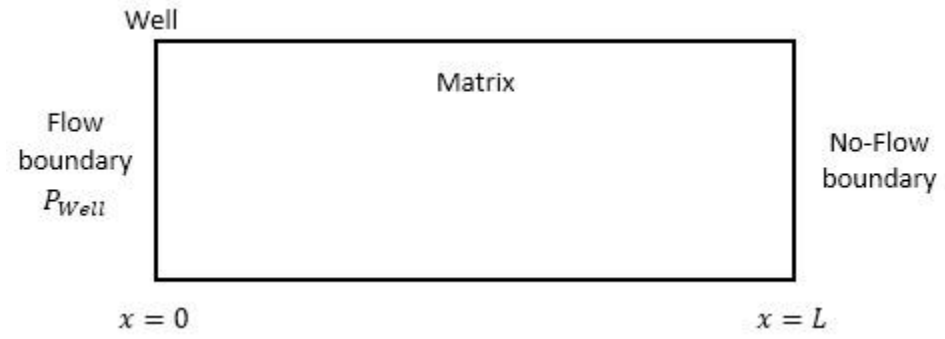

Figure 1 1D shale Matrix with pores inside

2.2. List of Assumptions

- The shale matrix initially contains methane (CH_4) component only, this is in form of free and adsorbed gas phases.
- The composition of free and adsorbed gas phases is assumed to be the same.
- There is no other phases such as water or oil presented.
- The pore geometry is assumed to be in the form of n-sphere shape.
- A solid volume inside the bulk volume is assumed to be constant.
- The adsorbed gas has a fixed density which is close to a liquid methane density.

2.3. Pore Volume Calculation

To calculate the porosity inside the shale matrix we need to have the pore volume. To obtain pore volume we use the volume of n-sphere pore (Evans 1947). This relation for a pore with radius R is

$$(R) = \frac{\pi^{\frac{n}{2}}}{\Gamma\left(\frac{n}{2}+1\right)} R^n \qquad 2.1$$

An n-sphere is the surface or boundary of an (n + 1)-dimensional ball. The full derivation of above formula (3.1) is shown in **Appendix A**. The Gamma function (Γ) is one commonly used extension of the factorial function to complex numbers. The definition and one property of this function is as follow

$$\Gamma(z) = \int_{x=0}^{\infty} x^{z-1} e^{-x} dx \qquad 2.2$$

$$\Gamma(n) = (n-1)! \qquad 2.3$$

By considering the volume of n-sphere pore in our 2-dimension matrix we obtain the surface area of a circle (πR^2), yet, we need the volume to be able to calculate the pore volume. To convert this n-volume formula to a 3D volume we use an assumedly constant conversion factor C (volume per n-volume). For n=1 this equals the cross section of the fracture, for n=2 it is the length of the cylinder, and for n=3 it equals 1. It is however assumed only to depend on n and constant otherwise.

We also know that the volume of n-sphere pore formula (2.1) is only for calculating one pore inside the matrix. Let N be the total number of pores per bulk volume. The total pore volume in our sample is then

$$V_p = NCV_n \tag{2.4}$$

The bulk volume of the sample (V_b) is the sum of pore and solid volume (V_s is constant).

$$V_b = V_p + V_s \tag{2.5}$$

Then the porosity at a given time is

$$\phi = \frac{V_p}{V_b} = \frac{NCV_n}{NCV_n + V_s} = \frac{V_n}{V_n + \frac{V_s}{NC}} \tag{2.6}$$

By assuming that we know the porosity at initial time, then

$$\phi_0 = \frac{NCV_n^0}{NCV_n^0 + V_s} = \frac{V_n^0}{V_n^0 + \frac{V_s}{NC}} \tag{2.7}$$

This helps us to determines the constant

$$\frac{V_s}{NC} = \frac{V_n^0}{\phi_0} - V_n^0 \tag{2.8}$$

And the porosity is as follow

$$\phi = \frac{V_n}{(V_n - V_n^0) + \frac{V_n^0}{\phi_0}} = \frac{\frac{V_n}{V_n^0}}{\left(\frac{V_n}{V_n^0} - 1\right) + \frac{1}{\phi_0}} \tag{2.9}$$

If we rewrite equation 2.9 using 2.1 and rearrange it to obtain current radius of the pores we will get the following equation

$$R^n = R_0^n \frac{\frac{1}{\phi_0} - 1}{\frac{1}{\phi} - 1} = R_0^n \frac{\phi(1-\phi_0)}{\phi_0(1-\phi)} \tag{2.10}$$

Equation 2.10 will gives us a relation between the current pore radius and original pore radius based on changes in porosity.

2.4. Mass Conservation

We define free gas volume per pore volume as free gas saturation

$$S_g = \frac{V_f}{V_p} \tag{2.11}$$

In our mass conservation calculation free and adsorbed gas is given by mass per gas volume (density) times gas volume per pore volume (saturation), then mass conservation can be described by

$$\begin{aligned}\left[\left(\rho_g S_g + \rho_a(1-S_g)\right)V_p\right]_{t+\Delta t} - \left[\left(\rho_g S_g + \rho_a(1-S_g)\right)V_p\right]_t \\ = \left(\rho_g \frac{u}{\phi} A_p\right)_x \Delta t - \left(\rho_g \frac{u}{\phi} A_p\right)_{x+\Delta x} \Delta t\end{aligned} \tag{2.12}$$

Where ρ_g and ρ_a are free and adsorbed gas density respectively in $[\frac{kg}{m^3}]$, u is velocity in $[\frac{m}{s}]$ and A_p is the surface area of the pore ($[m^2]$) which gas is flowing through. By writing pore volume in terms of surface area and length we get

$$\begin{aligned}\left[\left(\rho_g S_g + \rho_a(1-S_g)\right)A_p dx\right]_{t+\Delta t} - \left[\left(\rho_g S_g + \rho_a(1-S_g)\right)A_p dx\right]_t \\ = \left(\rho_g \frac{u}{\phi} A_p\right)_x \Delta t - \left(\rho_g \frac{u}{\phi} A_p\right)_{x+\Delta x} \Delta t\end{aligned} \tag{2.13}$$

Use that $A_p = \frac{A_s \phi}{(1-\phi)}$ where A_s is constant we can simplify 2.13 to

$$\begin{aligned}\left[\left(\rho_g S_g + \rho_a(1-S_g)\right)\frac{\phi}{(1-\phi)} dx\right]_{t+\Delta t} - \left[\left(\rho_g S_g + \rho_a(1-S_g)\right)\frac{\phi}{(1-\phi)} dx\right]_t \\ = \left(\rho_g \frac{u}{(1-\phi)}\right)_x \Delta t - \left(\rho_g \frac{u}{(1-\phi)}\right)_{x+\Delta x} \Delta t\end{aligned} \tag{2.14}$$

Which after more simplification we obtain the following mass conservation equation

$$\partial_t \left[\left(\rho_g S_g + \rho_a(1-S_g)\right)\frac{\phi}{(1-\phi)}\right] = -\partial_x \left(\rho_g \frac{u}{(1-\phi)}\right) \tag{2.15}$$

In equation we consider that the total pore volume is occupied by free gas V_f and adsorbed gas V_a

$$V_p = V_f + V_a \tag{2.16}$$

Also we will assume that we know the average gas density $\rho_{av} = \rho_g S_g + \rho_a(1-S_g)$. However, the distribution of the free gas saturations (S_g) is unknown.

Firstly, we will assume adsorbed gas has a fixed density (ρ_a similar to a liquid) and that the density of free gas ρ_g behaves according to the ideal gas law

$$\rho_g = \frac{pM}{R_g T} \qquad 2.17$$

Which p is the pressure of the free gas, R_g is the gas constant, T is absolute temperature and M stands for molecular weight.

We have now information about ρ_a and ρ_g, therefore, by implementing the isotherm and using relations 2.11 and 2.16, the distribution of the free gas saturations can be obtained.

2.5. Thickness of the Adsorption Layer

The release of adsorbed gas is commonly described by a pressure relationship which assumes that the gas attaches to the surface of the shale, and covers the surface as a single layer of gas (a monolayer). We want to derive a relation for the change in the thickness of this adsorbed layer.

First, in the simplest form we consider the sphere shape pores with only one layer of methane adsorbed (**Figure 2**) on the surface of the shale (no CO2 is presented here).

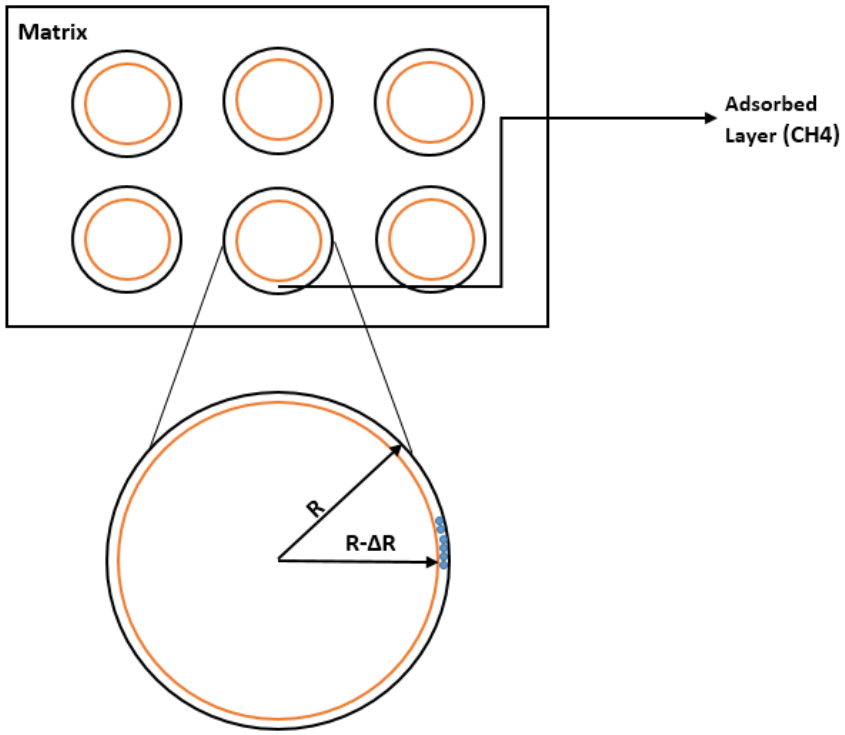

Figure 2 Adsorption layer thickness inside the pores.

The goal is to find the volume of adsorbed layer through two different approaches and calculations, then we find the layer thickness by comparing those two calculations.

The first approach is finding the volume of adsorbed layer based on geometric properties. If the pore radius is R, then the volume of n-sphere pore is obtained by the same relation 2.1. If we consider the layer thickness as ΔR, then, by using the same formula we can derive a volume only related to the adsorbed layer

$$V_{adsorbed\ layer} = V_{pore\ before\ adsorption} - V_{free\ gas} \quad 2.18$$

$$V_{adsorbed\ layer} = NC\frac{\pi^{\frac{n}{2}}}{\Gamma\left(\frac{n}{2}+1\right)}R^n - NC\frac{\pi^{\frac{n}{2}}}{\Gamma\left(\frac{n}{2}+1\right)}(R-\Delta R)^n \quad 2.19$$

$$V_{adsorbed\ layer} = NC\frac{\pi^{\frac{n}{2}}}{\Gamma\left(\frac{n}{2}+1\right)}\left[R^n-(R-\Delta R)^n\right] \quad 2.20$$

Where C is the constant conversion factor and is used to convert n-volumes to volumes. R is the pore 'radius' and $(R-\Delta R)$ is the effective radius for flow.

The release of adsorbed gas is commonly described by a pressure relationship called the Langmuir Isotherm. The Langmuir adsorption isotherm assumes that the gas attaches to the surface of the shale, and covers the surface as a single layer of gas (a monolayer).

The typical formulation of Langmuir isotherm is:

$$C_g = \frac{C_{max}\,p}{p_L+p} \quad 2.21$$

Which C_g is adsorbed gas in $[\frac{m^3}{kg}]$, C_{max} is the maximum amount of gas that can be adsorbed to shale at infinite pressure in $[\frac{m^3}{kg}]$, p is the pressure of the gas and p_L is the Langmuir pressure which is the pressure at which one half of the Langmuir volume can be adsorbed.

Let adsorption thickness ΔR reach a maximum thickness ΔR_{max} according to a Langmuir expression:

$$\Delta R = \Delta R_{max}\frac{p}{p_L+p} \quad 2.22$$

2.6. Porosity Relation

Transportation of shale gas in micro scale media is not following the conventional Darcy equation. It is instead influenced by factors like absorbed gas, pore pressure, pore size, and properties of porous media. Therefore, natural-property parameters of a reservoir (permeability and porosity) are no longer applicable for describing complex gas- transport mechanisms in shale reservoirs.

The porous medium in shale is a nanoscale medium that mainly consists of micro pores that has extremely low permeability (Hao, Cui et al. 2011). Gas flow in the shale matrix is subject to the diffusion of dissolved gas in kerogen and desorption from the pore walls. The flow mechanism of porous kerogen can be explained by Knudsen diffusion, surface diffusion and gas adsorption and desorption (Langmuir 1916, Javadpour, Fisher et al. 2007, Civan 2010, Akkutlu and Fathi 2012).

We can use the apparent porosity to be able to account for the presence of absorbed gas and free gas. Sheng and Javadpour have introduced the apparent porosity of the organic matter (Sheng, Javadpour et al. 2018).

$$\phi_{app} = \phi_{ini} e^{C_k(p_o - p_{ini})} + \mathcal{E}_s(1 - \phi_{ini} e^{C_k(p_o - p_{ini})}) C_a \frac{ZRT}{(p_L - p_o)} \qquad 2.23$$

Where ϕ is the porosity; C_k is the organic matter total compressibility in $[Pa^{-1}]$, $\mathcal{E}_{ks}$ is the proportion of solid matrix volume in the total interconnected matrix pore volume; C_a is the Langmuir volume on the organic matter surface in $[\frac{mol}{m3}]$, p_{ini} is the initial pressure of the shale gas reservoir in $[Pa]$. Z is the gas compressibility factor; R_g is the universal gas constant ($8.314\ [\frac{J}{K.mol}]$), T is the formation temperature in $[K]$, p_o is the pressure in organic matter (kerogen pressure) in $[Pa]$ and p_L is Langmuir's pressure in $[Pa]$.

However, the assumptions in Sheng and Javadpour's study were different compare to the assumptions in this work. The apparent porosity in their study considers the free gas and the adsorbed gas as different occupying elements, yet in our work, we calculate the total porosity for both free gas and adsorbed gas at the same time. This does not mean that the adsorbed gas is not being considered. We have already calculated the saturations to be able to account for the adsorbed gas.

The assumptions related to porosity calculation in our model is as follow:

- We consider overburden pressure and pore volume pressure as factors causing compaction, therefore, we expect total porosity to decrease due to compression of the matrix during natural depletion of shale gas reservoirs.
- For the free and adsorbed gas system in the pores inside the shale gas reservoir, we assume that it all behave as a tanker filled with water in which there is a big balloon full of gas inside it (**Figure 3** (TinkerCad 2020)). This is imaginary system is because we assume that the pressure inside the pore that holds the matrix is coming from the free gas (big balloon) which pushes the adsorbed gas layer on the wall (water inside the reservoir) and because the adsorbed gas molecules are incompressible, they can transfer the whole pressure from the free gas to the wall of the pores inside the matrix.

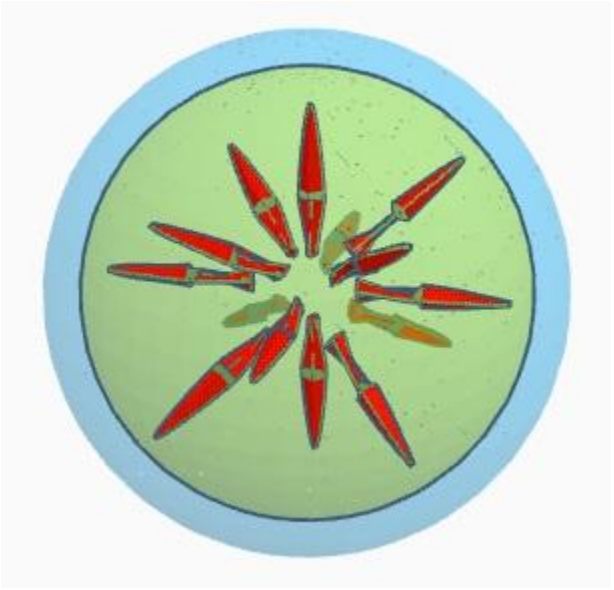

Figure 3 Imaginary model for pressure transfer through the adsorbed layer

Therefore in our porosity calculations we can consider the total porosity relation (free and adsorbed gas) which is a well-known relation between porosity and compressibility of the matrix.

$$\phi = \phi_0 e^{C_k(p-p_{ini})} \qquad 2.24$$

The relation above is the same as the first term of the RHS in 2.23 which is the pore volume occupied by free gas in per unit volume of rock.

2.7. Permeability Relation

Darcy equation is a simple equation that has been used in reservoir studies for many years. The mass conservation equation for a fluid flowing through a pore network is:

$$\frac{\partial \rho}{\partial t} = -\nabla \cdot (\rho u) \qquad 2.25$$

Where ρ is density, t is time and u is velocity. We can neglect the effect of gravity in gases because of their low density; hence, for the velocity term in pores (range of tens to hundreds of microns) the empirical Darcy's law can be written:

$$u = -\frac{k}{\mu}(\nabla p) \qquad 2.26$$

In which μ is fluid viscosity in $[\frac{Pa}{s}]$, k is absolute Darcy permeability and p is pressure. Now we can rewrite equation 2.25 as:

$$\frac{\partial \rho}{\partial t} = -[\nabla \cdot (\rho \left(\frac{k}{\mu}\nabla p\right))] \qquad 2.27$$

Equation 2.27 has been used widely as a general flow equation for a compressible fluid in conventional reservoirs. Here in this work, we also have a system that we would like to describe using the Darcy equation, but the physics of the problem are different. The Darcy permeability is not valid because the migration of shale gas in microscale media is strongly influenced by factors such as absorbed gas, pore pressure, pore size, and properties of porous media. Different modelling approaches can be implemented to model gas flow in nanopores, molecular dynamics (MD) (Bird and Brady 1994), direct simulation Monte Carlo (DSMC) (Karniadakis, Beskok et al. 2006), Burnett equation (Karniadakis, Beskok et al. 2006) and Lattice-Boltzmann (LB) (Hornyak, Dutta et al. 2008) are among these modelling solutions. These modelling schemes are computationally exorbitant and cannot be used for systems larger than a few microns. Therefore, we will use the apparent permeability term, which at the same time, enable us to distinguish from the Darcy equation.

The "apparent permeability" term has been used in recent years to describe gas transport in microscale pores for shale gas reservoirs. In 2009 Javadpour compared formulation for gas flow with the Darcy equation and then introduced an apparent-permeability model which couples viscous flow and Knudsen diffusion in nanopores. After this work, many scholars have developed numerous shale models based on Javadpour model. Apparent-permeability models now can be categories three types:

- Javadpour models based on the pore radius of porous media (Javadpour, Fisher et al. 2007). These models characterize intrinsic permeability, Knudsen diffusion coefficient, and slip factor and use pore size to propose coupled-flow equations considering viscous flow, slippage effect, Knudsen diffusion, and surface diffusion.
- Civan models based on Knudsen number (Civan 2010). These models apply the Beskok model (Beskok and Karniadakis 1999) to describe gas migration in porous media and use the Knudsen number to couple viscous flow and Knudsen diffusion.
- The Dusty-Gas Model (DGM) based on diffusion coefficient (Freeman, Moridis et al. 2011). In the DGM, apparent permeability is presented in the form of the Klinkenberg effect for one-component gas in shale gas reservoirs with viscous flow and Knudsen diffusion. This model couples molecular diffusion, Knudsen diffusion, and viscous flow in porous media.

Apparent permeability of shale gas reservoirs is affected by many factors. Pore pressure, reservoir temperature, surface roughness, and phase change are amongst some of these factors that has been studied in recent researches (Higashi, Ito et al. 1963, Zarragoicoechea and Kuz 2004, Chen, Cao et al. 2008).

There are some assumptions in deriving the apparent permeability model. These assumptions are as follow:

- The viscosity of the gas contained within the pores of shale is constant and the gas act as an ideal gas
- Shale matrix is saturated by gas
- Strain is much smaller compared with the matrix scale
- Rock matrix in shale is an isotropic, homogeneous and elastic continuum
- Isothermal condition

Knudsen number and flow regimes

To classify flow regimes in small pores of shale matrix, Knudsen number is commonly used. This number is a dimensionless parameter. The definition is "the ratio of molecular mean free path, with a characteristic length (average pore radius)", and is given as

$$Kn = \frac{\lambda}{R_h} \tag{2.28}$$

Which R_h is the mean hydraulic radius of flow tubes or paths formed during flow through porous media and λ is the mean-free-path of molecules and is expressed as (Loeb 2004)

$$\lambda = \frac{\mu}{p}\sqrt{\frac{\pi R_g T}{2M}} \tag{2.29}$$

where μ is the viscosity of gas in $[Pa.s]$, p is the absolute gas pressure in $[Pa]$, $R_g = 8314\ [\frac{JK}{kmol}]$ is the universal gas constant, T is the absolute temperature in $[K]$, and M is the molecular weight of gas in $[\frac{kg}{mol}]$.

The hydraulic radius R_h of flow tube is given by (Carman 1956, Civan 2007)

$$R_h = 2\sqrt{2}\sqrt{\frac{k_\infty \tau_h}{\phi}} \tag{2.30}$$

Where τ_h is the tortuosity and ϕ is the porosity of porous media.

Figure 4 illustrates different types of flow regimes in a micro channel. Flow regimes can be classified into the following types based on the Knudsen number (Ziarani and Aguilera 2012)

1. Viscous or continuum flow ($Kn < 0.01$), in this condition, conventional fluid dynamics are applicable. The mean free path of gas is much smaller than the pore size of the porous medium, therefore the probability of collisions between molecules is much higher than collisions between the molecules and the pore walls, and the gas transport is mainly governed by viscous flow. In this flow regime, the apparent permeability for gas is the same as the intrinsic permeability because slippage effect is pretty small. Therefore, Darcy's equation is generally adopted in the case of fluid flow for a porous medium.
2. Slip flow ($0.01 < Kn < 0.1$), the pore size of the porous medium is still larger than the mean free path of gas molecules, the probability of collisions between molecules is still higher than collisions between the molecules and the pore walls. And conventional flow equations can be applicable with some modification. This flow regime occurs when the gas molecules slipping at the solid interface.
3. Transition flow ($0.1 < Kn < 10$), in this flow regime, the collisions between the molecules and the pore walls become more important and the gas transport is mainly governed by diffusion flows. Generally, the traditional fluid dynamics equations start to fail. The higher the Knudsen number, the higher the chance of failure.

4. Knudsen's (free molecular) flow ($10 < Kn$) the collisions between the molecules and the pore walls become more important and the gas transport is mainly governed by Knudsen diffusion. This regime usually occurs at system like kerogen with low pressures or very tight pore throats.

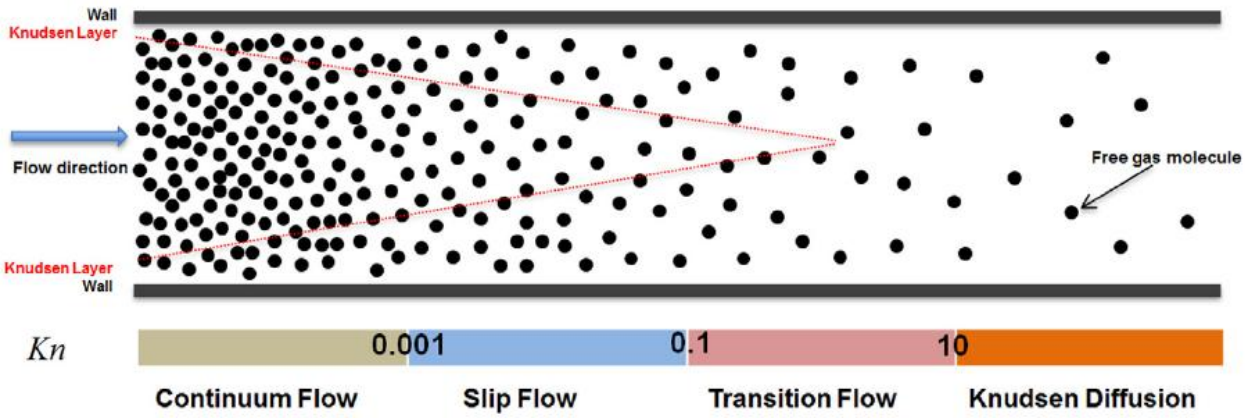

Figure 4 Four different types of flow regimes in a micro channel. In this diagram an infinite long micro channel is assumed with a high pressure difference between inlet and outlet. The height of micro channel is also magnified (Yuan and Rahman 2016).

Beskok and Karniadakis (Beskok and Karniadakis 1999) developed a rigorous equation for volumetric flow in a microtube. They showed that the equation is valid for the entire Knudsen's range and is second order accurate for the slip flow regime. Beskok and Karniadakis' equation is as follows:

$$q = [1 + \alpha(kn)Kn]\left[1 + \frac{4Kn}{1 - bKn}\right]\frac{\pi r^4}{8\mu}\frac{\Delta P}{L} \qquad 2.31$$

Where L is the pipe length, r is the pipe radius, Kn Knudsen number, ΔP the pressure drop along the pipe length, α dimensionless rarefaction coefficient, which is a function of Knudsen number, b a constant (which is equal to -1 for slip flow), and μ the dynamics viscosity of fluid.

If we relate the equation 2.31 to Darcy's equation, we will have

$$q = f_c\, q_{Darcy} \qquad 2.32$$

Where f_c is a Knudsen's correction factor given by Beskok and Karniadakis and Florence (Beskok and Karniadakis 1999, Florence, Rushing et al. 2007).

$$f_c = [1 + \alpha(kn)Kn]\left[1 + \frac{4Kn}{1 - bKn}\right] \qquad 2.33$$

Using a similar analogy, Apparent permeability is related to absolute permeability (k_∞) using:

$$K_a = f_c\, k_\infty \qquad 2.34$$

Where k_∞ denotes the liquid permeability of porous media given by

$$k_\infty = \frac{\phi(R-\Delta R)^2}{8\,\tau_h} \tag{2.35}$$

Below is the explicit form of permeability adjustment, done by Florence et al. for flow through capillary tubes. It only relies on the Knudsen number and the intrinsic permeability of the porous medium (Florence, Rushing et al. 2007):

$$K_a = k_\infty\,[1+\alpha(K_n)K_n]\left[1+\frac{4K_n}{1+K_n}\right] \tag{2.36}$$

As we had before, the function $\alpha(kn)$ is a rarefaction parameter, which is a dimensionless adjustment parameter as follows

$$\alpha(K_n) = \frac{128}{15\pi^2}\tan^{-1}[4.0{K_n}^{0.4}] \tag{2.37}$$

The constant values in 2.37 come from the derivation of Karniadakis and Beskok for flow through a bundle of capillary tubes.

In 2.36 K_n is Knudsen number which is defined as follow

$$K_n = \frac{\mu Z}{p(R-\Delta R)}\sqrt{\frac{\pi R_g T}{2M_g}} \tag{2.38}$$

At the end, the gas velocity term in pores can be described macroscopically by a Darcy-type gradient-law of flow, where the flow is assumed proportional to the pressure gradient (∇p) given by

$$u = -\frac{K_a}{\mu}(\nabla p) \tag{2.39}$$

Which K_a is the apparent permeability of gas in the matrix and μ the gas viscosity, which is set constant.

2.8. Summary of the model

In this section we are summarizing all relations and formulas that we need to implement together in our model to solve the mass conservation equation (2.15).

The main equation to solve is equation 2.15 which is the mass conservation equation:

$$\partial_t\left[\left(\rho_g S_g + \rho_a(1-S_g)\right)\frac{\phi}{(1-\phi)}\right] = -\partial_x\left(\rho_g\frac{u}{(1-\phi)}\right) \tag{2.40}$$

We have the density relations from 2.17

$$\rho_g = \frac{pM}{R_g T}\,,\ \rho_a = constant \tag{2.41}$$

The gas velocity term is also as follow

$$u = -\frac{K_a}{\mu}\partial_x p \tag{2.42}$$

Using these two relations and with some simplification equation 2.15 will turn to

$$\partial_t \left[\left(pS_g + \frac{R_g T\ \rho_a}{M}\left(1 - S_g\right)\right)\frac{\phi}{(1-\phi)}\right] = \frac{1}{\mu}\partial_x\left(\frac{pK_a}{(1-\phi)}\partial_x p\right) \tag{2.43}$$

We have free gas saturation formulas from 2.11

$$S_g = \frac{V_f}{V_p},\ S_g + S_a = 1 \tag{2.44}$$

Based on porosity relation and volume of the n-sphere pore (2.9 and 2.1) we drive the relation for radius change as a function of porosity and initial porosity

$$R^n = R_0^n \frac{\frac{1}{\phi_0} - 1}{\frac{1}{\phi} - 1} = R_0^n \frac{\phi(1-\phi_0)}{\phi_0(1-\phi)} \tag{2.45}$$

Which ΔR comes from 2.22

$$\Delta R = \Delta R_{max}\frac{p}{p_L + p} \tag{2.46}$$

Then, we can rewrite the saturations as

$$S_g = \frac{V_f}{V_p} = \frac{\left(R - \Delta R_{max}\frac{p}{p_L + p}\right)^n}{R^n} = (1 - \frac{\Delta R_{max}}{R}\frac{p}{p_L + p})^n = (1 - \frac{\Delta \mathrm{R}}{R})^n \tag{2.47}$$

The apparent permeability comes from 2.36

$$K_a = \ k_\infty\left[1 + \alpha(K_n)K_n\right]\left[1 + \frac{4K_n}{1 + K_n}\right] \tag{2.48}$$

Where K_n denotes for the Knudsen number

$$K_n = \frac{\mu Z}{p(R - \Delta R_{max}\frac{p}{p_L + p})}\sqrt{\frac{\pi R_g T}{2M_g}} \tag{2.49}$$

And k_∞ is the absolute permeability

$$k_\infty = \frac{\phi S_g (R - \Delta R)^2}{8\,\tau_h} \tag{2.50}$$

Which τ_h is the tortuosity of the porous medium, and $\alpha(K_n)$ is referred to as the rarefraction parameter

$$\alpha(K_n) = \frac{128}{15\pi^2}\tan^{-1}\left[4.0{K_n}^{0.4}\right] \quad 2.51$$

We also have the porosity relation from 2.24

$$\phi = \phi_0 e^{C_k(p-p_{ini})} \quad 2.52$$

2.9. Operator Splitting

We solve the transport system (2.53) with all the constrains mentioned in **Section 2.8** (F ree gas saturation, Apparent permeability and Porosity relation) using an operator splitting approach (Andersen, Evje et al. 2014, Agista, Andersen et al. 2019). This method is particularly useful for solving complex systems by dividing them into easily solved subsystems. In this case we have a mass conservation equation as follow

$$\partial_t\left[\left(pS_g + \frac{R_g T\ \rho_a}{M}\left(1-S_g\right)\right)\frac{\phi}{(1-\phi)}\right] = \frac{1}{\mu}\partial_x\left(\frac{pK_a}{(1-\phi)}\partial_x p\right) \quad 2.53$$

For simpler notation we can write

$$\partial_t\left[\left(pS_g + \hat{a}\left(1-S_g\right)\right)\frac{\phi}{(1-\phi)}\right] = \frac{1}{\mu}\partial_x(D\partial_x p) \quad 2.54$$

Which

$$D = \frac{p\ K_a}{(1-\phi)} \quad 2.55$$

And

$$\hat{a} = \frac{RT\ \rho_a}{M} \quad 2.56$$

We split the coupled system into the following two subsystems

2.9.1. No Adsorption

We only consider advective flow of free gas, while adsorption of gas is held constant

$$\partial_t\left(\hat{a}\left(1-S_g\right)\frac{\phi}{(1-\phi)}\right) = 0 \quad 2.57$$

The total simulation time T_{total} is divided into splitting time steps ΔT. This system (2.9.1) is solved over this period of time (ΔT) before the masses are locally distributed in the next system (2.9.2). The splitting time step must be selected small enough to allow the different systems to participate frequently enough to provide relevant information in each other's solution procedure. We solve

the transport system over a time period equal to the splitting step (ΔT), knowing that the adsorption content is held fixed with time, (2.57). Assuming that only pressure changes over the time step, from (2.53) we have

$$S_g \frac{\phi}{(1-\phi)} \partial_t(p) = \frac{1}{\mu} \partial_x(D \partial_x p) \qquad 2.58$$

2.9.2. No Flow

We assume no advective flow. While preserving the mass, the gas is redistributed locally between free gas and adsorbed form to assure isotherm equilibrium.

$$\partial_t \left[\left(p S_g + \hat{a} \left(1 - S_g\right) \right) \frac{\phi}{(1-\phi)} \right] = 0 \qquad 2.59$$

We adjust p and $\hat{a}_g$ locally to be in equilibrium, as given by the adsorption isotherm. The conserved property is $\left(p_g S_g + \hat{a} \left(1 - S_g\right) \right) \frac{\phi}{(1-\phi)}$. Because the isotherm is evaluated most easily with absolute pressure, we perform the equilibration in absolute units

$$M = \left(p_{new} S_g(p_{old}) + \hat{a} \left(1 - S_g(p_{old})\right) \right) \frac{\phi(p_{old})}{(1-\phi(p_{old}))} \qquad 2.60$$

Which, M is a conserved property with units of pressure. After obtaining M using the updated pressure we want to re-update the pressure also by considering adsorption term. Because the pressure obtained from matrix diffusion of free gas has not altered other properties like porosity or saturation, so the pressure and those properties are not in equilibrium and require adjustment. This adjusted pressure (p_{adj}) can be obtained from the same relation like 2.60 and mass conservation. This means we will keep the M constant and we will solve the equation, this time for (p_{adj}). For finding p_{adj} we have to solve equation 2.61. To solve this equation we implement an iteration method using two initial guesses and the half splitting technique. After this, we have an adjusted pressure (p_{adj}) and the corresponding properties that must add to the same amount M.

$$f(p_{adj}) = \left(p_{adj} S_g(p_{adj}) + \hat{a} \left(1 - S_g(p_{adj})\right) \right) \frac{\phi(p_{adj})}{\left(1 - \phi(p_{adj})\right)} - M \qquad 2.61$$

2.10. Discretization

Assuming the matrix is discretized into $i = 1{:}\, N_x$ cells. For equation (2.58) and for central cell (i) in the matrix we have

$$S_g \frac{\phi}{(1-\phi)} \frac{p_i^{n+1} - p_i^n}{\Delta t} = \frac{1}{\mu} \frac{(D \partial_x p)_{i+1/2} - (D \partial_x p)_{i-1/2}}{\Delta x} \qquad 2.62$$

With the flux defined by

$$(D\partial_x p_g)_{i+1/2} = \frac{2}{\frac{1}{D_{i+1}} + \frac{1}{D_i}} \frac{p_{i+1} - p_i}{\Delta x} \quad 2.63$$

$$(D\partial_x p_g)_{i-1/2} = \frac{2}{\frac{1}{D_i} + \frac{1}{D_{i-1}}} \frac{p_i - p_{i-1}}{\Delta x} \quad 2.64$$

At the starting cell for equation (2.62) we have

$$S_g \frac{\phi}{(1-\phi)} \frac{p_1^{n+1} - p_1^n}{\Delta t} = \frac{1}{\mu} \frac{(D\partial_x p)_{3/2} - (D\partial_x p)_{1/2}}{\Delta x} \quad 2.65$$

The matrix flux term at this interface is evaluated by

$$(D\partial_x p)_{3/2} = \frac{2}{\frac{1}{D_2} + \frac{1}{D_1}} \frac{p_2 - p_1}{\Delta x} \quad 2.66$$

$$(D\partial_x p)_{1/2} = \frac{2}{\frac{1}{D_1} + \frac{1}{\infty}} \frac{p_1 - p_{well}}{\Delta x/2} = 2D_1 \frac{p_1 - p_{well}}{\Delta x/2} \quad 2.67$$

At the starting cell for equation (2.62) we have

$$S_g \frac{p_{N_x}^{n+1} - p_{N_x}^n}{\Delta t} = \frac{1}{\mu} \frac{(D\partial_x p)_{N_x+1/2} - (D\partial_x p)_{N_x-1/2}}{\Delta x} \quad 2.68$$

The matrix fluxes at the matrix outer boundary $x = L$ are set to zero

$$(D\partial_x p)_{N_x+1/2} = 0 \quad 2.69$$

$$(D\partial_x p)_{N_x-1/2} = \frac{2}{\frac{1}{D_{N_x}} + \frac{1}{D_{N_x-1}}} \frac{p_{N_x} - p_{N_x-1}}{\Delta x} \quad 2.70$$

2.11. Stability Criteria

The stability condition in a finite difference scheme is satisfied when the effect of an error made in any stage of calculation is not propagated into larger errors in the next stages of calculation. This means that the local perturbations are not magnified by further calculations. A difference scheme can be examined for stability by substituting into it error values of the solution (see **Appendix B**).

The pressure is supposed to act in a diffusive way and drive the changes in the mass, therefore, we should avoid oscillation in pressure behavior to satisfy the stability. For instance, if we select a too large time step, too much gas will be transported inside the cell, and we may observe oscillation in the pressure profile. In three adjacent cells in the matrix $(i-1, i, i+1)$ the stability means

that; in each calculation step, the pressure change in the cell i should not be more than one-half of the maximum difference in pressure between cell i and its neighbors' cells at each time step.

$$|p_i^{n+1} - p_i^n| < \frac{1}{2}\max(|p_{i+1} - p_i|)$$
$$|p_i^{n+1} - p_i^n| < \frac{1}{2}\max(|p_i - p_{i-1}|) \quad 2.71$$

This allows selecting of subsequently higher time steps.

2.12. Original and Current Gas in Place and Gas Recovery

Both original gas in place ($OGIP$) and current gas in place ($GCIP$) is calculated according to the mass of free gas in the matrix (M_1) and mass of adsorbed gas in the matrix (M_2). These masses are evaluated over the length of the core sample.

If we consider relation 2.53 as the mass conservation equation, we can write for M_1 and M_2 in one cell as follow

$$M_1 = pS_g \frac{\phi}{(1-\phi)} \quad 2.72$$

$$M_2 = \frac{R_g T\ \rho_a}{M}\left(1 - S_g\right)\frac{\phi}{(1-\phi)} \quad 2.73$$

As it can be seen the unit of mass is in pressure units. If all the parameters in 2.72 and 2.73 are set at the initial condition, the result will be the mass of free and adsorbed gas at initial condition. Then the original gas in place is achieved by adding these two amounts.

$$OGIP = M_1 + M_2 \quad 2.74$$

At later time steps, after evaluating p_{adj} and updating other parameters based on that pressure, we can calculate the mass of free and adsorbed gas in those time steps using the same formula but updated values.

$$M_1 = p_{adj}S_g(p_{adj})\frac{\phi(p_{adj})}{\left(1-\phi(p_{adj})\right)} \quad 2.75$$

$$M_2 = \frac{R_g T\ \rho_a}{M}\left(1 - S_g(p_{adj})\right)\frac{\phi(p_{adj})}{\left(1-\phi(p_{adj})\right)} \quad 2.76$$

The ($GCIP$) is calculated

$$GCIP = M_1 + M_2 \quad 2.77$$

The recovery factor RF is evaluated as

$$RF = 1 - \frac{GCIP}{OGIP} \tag{2.78}$$

We also introduce the ultimate recover factor and the fraction of ultimate recovery factor as follow

$$RF_{\infty} = 1 - \frac{GCIP(p_{well})}{OGIP} = \frac{OGIP - GCIP(p_{well})}{OGIP} \tag{2.79}$$

$$RF_{frac} = \frac{RF}{RF_{\infty}} = \frac{OGIP - GCIP}{OGIP - GCIP(p_{well})} \tag{2.80}$$

Ultimate recovery factor is the recovery when the pressure has uniformly reached the well pressure. Fraction of ultimate recovery factor is the ratio of the recovery at each pressure to the ultimate recovery factor.

2.13. Averaging Properties

To present an understandable values for each property we use average properties. This averaging is done after each time step; therefore we can record the average values during the entire simulation time.

After solving the mass conservation equation (2.53) and finding p in each time step we update porosity, apparent permeability, free gas saturation, and thickness. However, as we are calculating these properties in small elements in the core we use averaging methods to report a unique value of each property over the entire length of the sample at a specific time.

2.13.1. Average Porosity

As we assumed in our model, the solid volume inside the sample is constant, therefore, the pore volume and bulk volume in each cell is as follow

$$V_{pi} = V_s \frac{\phi_i}{1 - \phi_i} \tag{2.81}$$

$$V_{bi} = V_s \frac{1}{1 - \phi_i} \tag{2.82}$$

We have the total pore volume and bulk volume as follow

$$V_{ptot} = V_s \sum_{i=1}^{N} \frac{\phi_i}{1 - \phi_i} \tag{2.83}$$

$$V_{btot} = V_s \sum_{i=1}^{N} \frac{1}{1 - \phi_i} \tag{2.84}$$

The ratio between the two volumes above will be the average porosity along the entire core sample

$$\bar{\phi} = \frac{V_{ptot}}{V_{btot}} = \frac{\sum_{i=1}^{N} \frac{\phi_i}{1-\phi_i}}{\sum_{i=1}^{N} \frac{1}{1-\phi_i}} \quad 2.85$$

2.13.2. Average Free gas Saturation

The volume of free gas in each cell and in the entire core sample is as follow

$$V_{gi} = V_s S_{gi} \frac{\phi_i}{1-\phi_i} \quad 2.86$$

$$V_{gtot} = V_s \sum_{i=1}^{N} \frac{S_{gi}\phi_i}{1-\phi_i} \quad 2.87$$

Also, the volume of pore space in each cell and the entire core sample follow equation 2.81 and 2.83. Using all the equations above, the average free gas saturation of free gas along the core sample is

$$\bar{S}_g = \frac{V_{gtot}}{V_{ptot}} = \frac{\sum_{i=1}^{N} \frac{S_{gi}\phi_i}{1-\phi_i}}{\sum_{i=1}^{N} \frac{\phi_i}{1-\phi_i}} \quad 2.88$$

2.13.3. Average Apparent Permeability

For apparent permeability we have used the common harmonic averaging method

$$\overline{K_a} = \frac{N}{\sum_{i=1}^{N} \frac{1}{K_{a_i}}} \quad 2.89$$

2.13.4. Average Free gas and Adsorbed gas Mass

To show the average mass for free and adsorbed gas at each time step we have used relation 2.53 and derived the following relations

$$\bar{M}_1 = \frac{1}{N} \sum_{i=1}^{N} pS_g \frac{\phi}{(1-\phi)} = \frac{1}{N} \bar{\phi}\, \bar{p}\bar{S}_g \sum_{i=1}^{N} \frac{1}{1-\phi_i} = \bar{p}\bar{S}_g \frac{\bar{\phi}}{1-\bar{\phi}} \quad 2.90$$

$$\begin{aligned}\bar{M}_2 = \frac{R_g T\ \rho_a}{M}\ \ & \frac{1}{N}\sum_{i=1}^{N}\left(1-S_g\right)\frac{\phi}{(1-\phi)} \\ &= \frac{R_g T\ \rho_a}{M}\ \left[\frac{1}{N}\sum_{i=1}^{N}\frac{\phi_i}{1-\phi_i} - \frac{1}{N}\bar{S}_g\sum_{i=1}^{N}\frac{\phi_i}{1-\phi_i}\right] \\ &= \frac{R_g T\ \rho_a}{M}\ \left[\frac{1}{N}\bar{\phi}\sum_{i=1}^{N}\frac{1}{1-\phi_i} - \frac{1}{N}\bar{S}_g\bar{\phi}\sum_{i=1}^{N}\frac{1}{1-\phi_i}\right] \\ &= \frac{R_g T\ \rho_a}{M}\ \left[\bar{\phi}\left(1-\ \bar{S}_g\right)\right]\frac{1}{N}\sum_{i=1}^{N}\frac{1}{1-\phi_i} \\ &= \frac{R_g T\ \rho_a}{M}\ \left[\frac{\bar{\phi}}{1-\bar{\phi}}\left(1-\ \bar{S}_g\right)\right]\end{aligned} \qquad 2.91$$

Where we have used

$$\begin{aligned}\frac{1}{1-\bar{\phi}} &= \frac{1}{1-\dfrac{\sum_{i=1}^{N}\dfrac{\phi_i}{1-\phi_i}}{\sum_{i=1}^{N}\dfrac{1}{1-\phi_i}}} = \frac{\sum_{i=1}^{N}\dfrac{1}{1-\phi_i}}{\sum_{i=1}^{N}\dfrac{1}{1-\phi_i} - \sum_{i=1}^{N}\dfrac{\phi_i}{1-\phi_i}} \\ &= \frac{\sum_{i=1}^{N}\dfrac{1}{1-\phi_i}}{\sum_{i=1}^{N}\dfrac{1-\phi_i}{1-\phi_i}} = \frac{\sum_{i=1}^{N}\dfrac{1}{1-\phi_i}}{N}\end{aligned} \qquad 2.92$$

2.13.5. Average Pressure

The average pressure along the core length at each time step is calculated from the following relation

$$\bar{p_g} = \frac{\sum_{i=1}^{N} p_{gi} S_{gi}\dfrac{\phi_i}{(1-\phi_i)}}{\sum_{i=1}^{N} S_{gi}\dfrac{\phi_i}{(1-\phi_i)}} \qquad 2.93$$

3. Simulation Result and Discussion

The function of the model is discussed in this section. The sensitivity of the model to different parameters is considered. We will see how different parameters related to both gas and matrix will affect pressure profile, the amount of free and adsorbed gas, and also recovery profile. We will also visualize free gas saturation alongside the core sample at different percentages of gas recovery factor. Gas recovery factor is reported as the produced fraction of the gas initially in place. Other distributions alongside the core sample, such as apparent permeability or thickness layer will also be discussed.

The mass conservation equation is solved by the operator splitting technique using MathWorks' MATLAB. This means that we first, solve the equation to find the updated pressure alongside the core in the new time step, then we adjust the other variables by distributing the local masses (in pressure units) between the free and adsorbed gas. Finally, we adjust the updated pressure and by using this value we can also update other parameters which are a function of pressure, such as free gas saturation, porosity, and apparent permeability.

The operator splitting time step was selected in a way to ensure that we will achieve an adequate frequency for switching between the two solvers functions in our MATLAB MainFile manuscript. The x-axis was discretized into 20 equal cells for all the simulation cases, and 15000 steps were chosen to perform mathematical calculations (For more explanations, see **Appendix C**).

3.1. Model Input

The model input parameters that we used for the base case are described in **Table 1**. The table also includes gas and rock properties. The Input parameters are taken from (Yu, Sepehrnoori et al. 2016) and they represent Marcellus Shale. All other parameters are held constant and equal to the base case unless otherwise stated.

Table 1 Input parameters used for reference case simulations.

Parameters	Value	Units
Well bottom hole pressure, P_{well}	$1.724 * 10^6$	Pa
Initial matrix pressure, P_{ini}	$3.447 * 10^7$	Pa
Real gas deviation factor (ideal gas), Z	1	–
Gas constant, R_g	8.314	J/mol
CH_4 viscosity, μ	$1.84 * 10^{-5}$	Pa.s
Matrix length, L	10	m
Initial pore radius, R_0	100	nm
Reservoir temperature, T	323.15	K
Tortuosity of rock, τ	1.51	-
Molar weight of CH_4	$16.04 * 10^{-3}$	kg/mol

3.2. Static Model Behavior

By choosing some of our base case parameters, we systematically varied some of the settings to study their effect as a function of pressure. We considered a pressure range of $3.447 * 10^7$ down to $1.724 * 10^6$, representing the initial reservoir pressure and well pressure, respectively. We distributed the pressures linearly to obtain a pressure profile during production. All the following results are based on this linear pressure distribution.

3.2.1. Role of Compressibility

We can see from 2.52 that compressibility has an enormous influence on porosity. **Figure 5** shows the effect of different compressibility values on porosity evolution during the pressure drop, it also contains the case when there is no compaction effect considered.

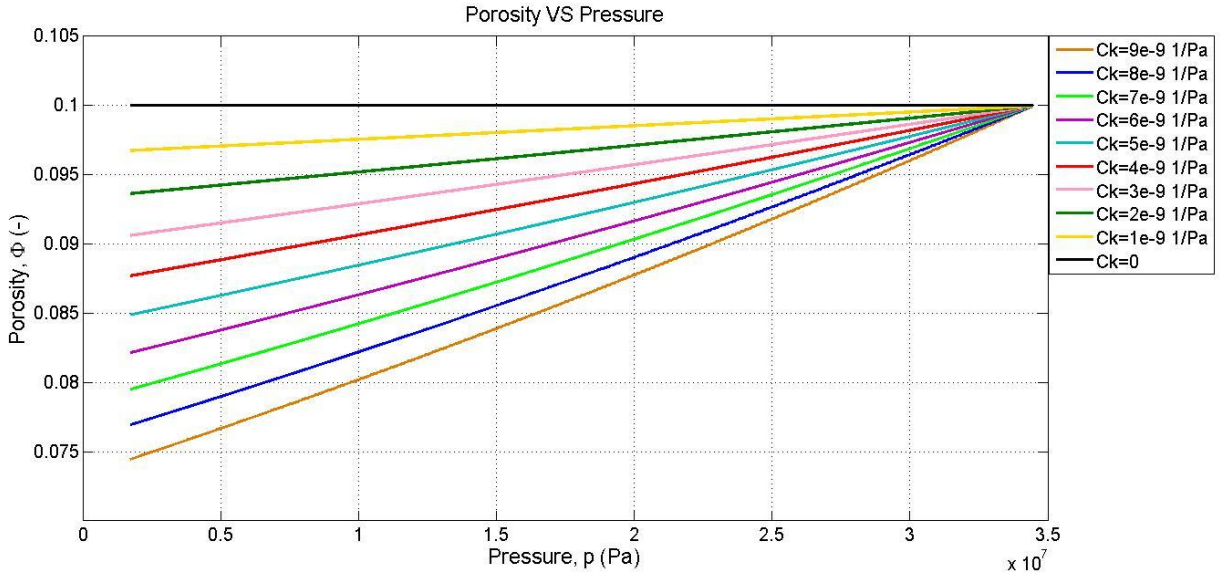

Figure 5 Porosity as a function of pressure ($\phi(p)$, equation 2.52) for different Compressibility values. Black line: when there is zero compressibility. Color lines: the effect of different compressibility factor on porosity profile.

When there is zero compressibility, the porosity will remain constant with pressure reduction. Porosity can decreases down to 25% of initial value, as the pressure reduces for the case with the compressibility of $9 * 10^{-9}$ $[\frac{1}{Pa}]$. Higher compressibility results in faster porosity decline as it appears in an exponential function (2.52). Porosity appears in pore radius relation and permeability relation (2.45 and 2.50) in our model and the figure indicates the importance of considering the compressibility in our dynamic simulation. As it is shown in some cases the porosity can reduce up to 25 percent of initial porosity which presumably has a significant impact on gas production. We chose a compressibility range from the work of (Davudov and Moghanloo 2018). We considered total pore compressibility of ($6 * 10^{-9}$ $[\frac{1}{Pa}]$) during our dynamic simulation. This value for compressibility results in 18% drop in porosity. It should be noted that the percentage of pore shrinkage may vary for different shale plays. Reservoir compaction can assist production, however, it should be noted that at some shale plays it may tend to cause pore closure due to reduction in pore radius.

3.2.2. Role of Initial Porosity

It is crucial to investigate the effect of initial porosity on the radius change during production. In other words, we want to see when porosity starts to influence the radius and, therefore, the portion of pore space covered by the adsorbed phase. For this purpose we plotted $\Delta R/R$ as a function of pressure (**Figure 6**). The value of $\Delta R/R$ shows the ratio of adsorption layer thickness to the pore radius at each pressure.

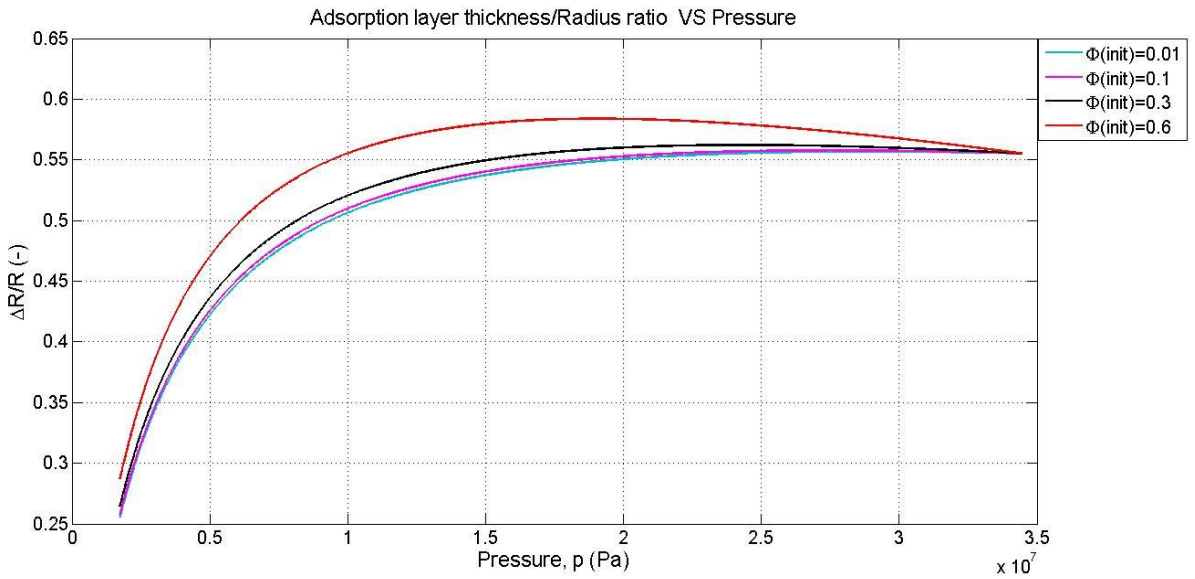

Figure 6 Ratio of adsorption layer thickness to the pore radius as a function of pressure ($\Delta R/R$ (p), equation 2.45 and 2.22) for different initial porosity values.

Here in this study, the initial porosity only affects the pore radius size (equation 2.45). From **Figure 6**, we can see that as initial porosity increases, the pore radius tends to reduce more, and as a result, the value of $\Delta R/R$ can get closer to its maximum. In low porosity range (Shale porosity range), we can see that the ratio of $\Delta R/R$ stays steady until we reach lower pressure values. This indicates that the decline in pore radius and adsorption layer thickness is happening at a similar rate at the beginning of the production. After we reach low pressures, the adsorption layer thickness declines rapidly while the pore radius decreases at the same rate. This is consistent with what is shown in **Figure 7**.

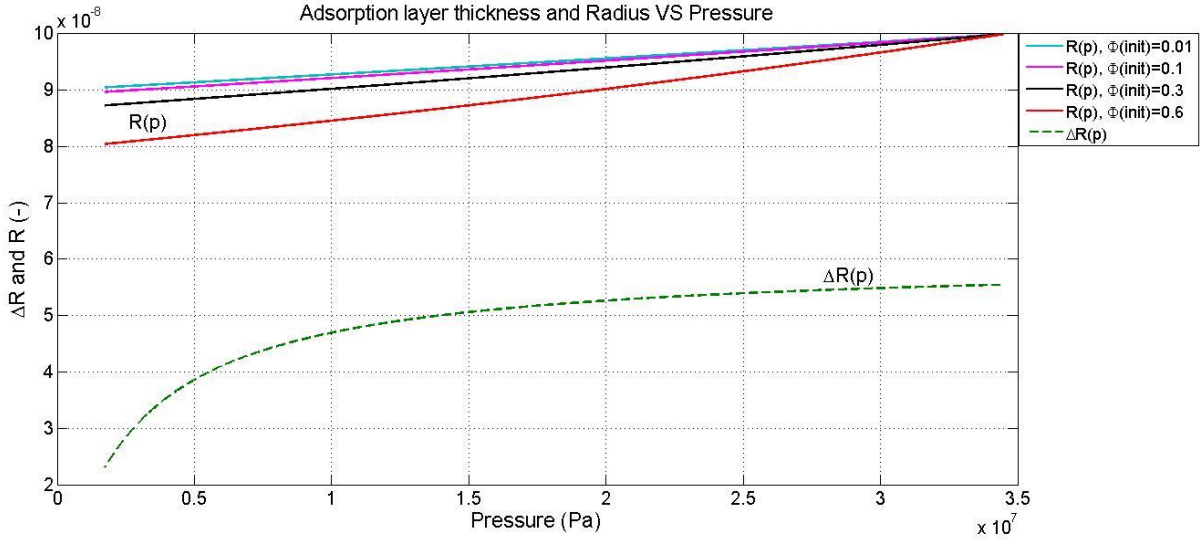

Figure 7 Ratio of adsorption layer thickness and the pore radius as a function of pressure ($\Delta R(p)$ and $R(p)$, equation 2.45 and 2.22) Solid lines:$R(p)$, Dash lines: $\Delta R(p)$.

3.2.3. Role of N-Sphere Geometry and Dimensional Boundary

One of the novel aspects of our study is how we define the pore space geometry. Therefore, it is crucial to study the effect of the dimensional boundary of the n-sphere pore volume (n). As we mentioned in **Chapter 2**, an n-sphere is the surface or boundary of an $(n + 1)$ - dimensional ball. In **Figure 8**, we can see different free gas saturation profiles for different values of n.

In principal (n) in our model is a number that describes the average pore shape, in other words, pore shapes in our core sample can be of any kind and if some are spheres and some are cylinders or straight fractures, any number can be representative of the dimensional boundary. It can be any real number, which is why we studied different cases with the average dimensional boundary of 1 to 3.

In **Figure 8**, we can see that as the shapes of all pore spaces approach straight fractures $(n = 1)$, we have higher free gas saturations. This is due to the unique arrangement and packing of the pore spaces inside the core that results in high saturation of free gas. In contrast, as we assign higher values to n $(n = 3)$, it means most of the pores are in the shape of spheres and cylinders, which can have less free gas saturation due to of poorly packed pore spaces in the matrix.

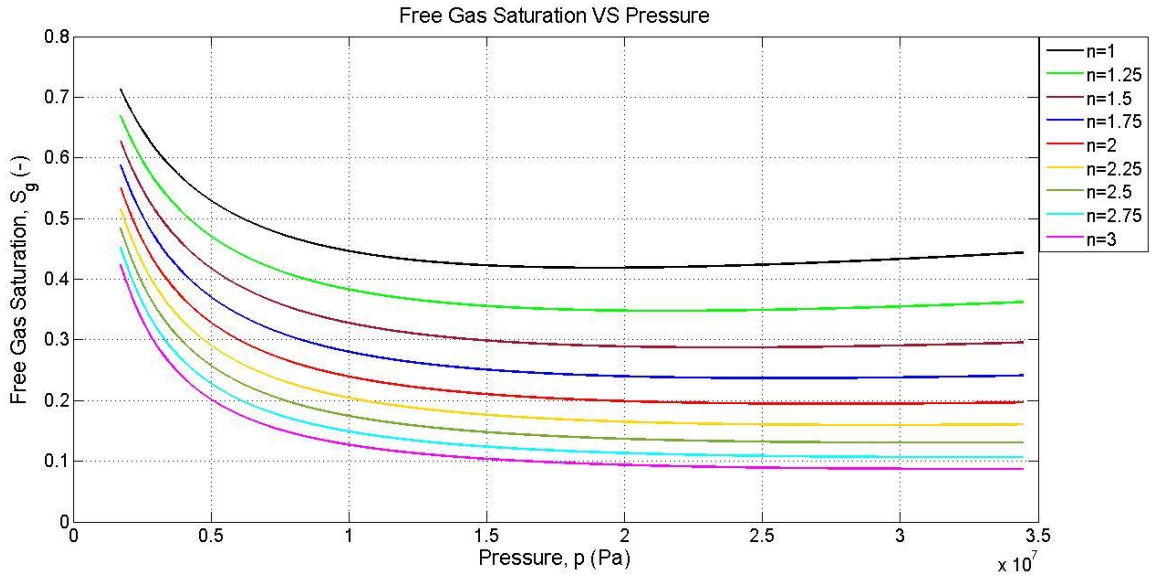

Figure 8 Free gas saturation as a function of pressure for different dimensional boundary of the pore spaces ($S_g(p)$ equation 2.47).

In **Figure 9**, we can see the effect of the dimensional boundary on apparent permeability. As expected, the same behavior is shown for apparent permeability as it is directly related to free gas saturation.

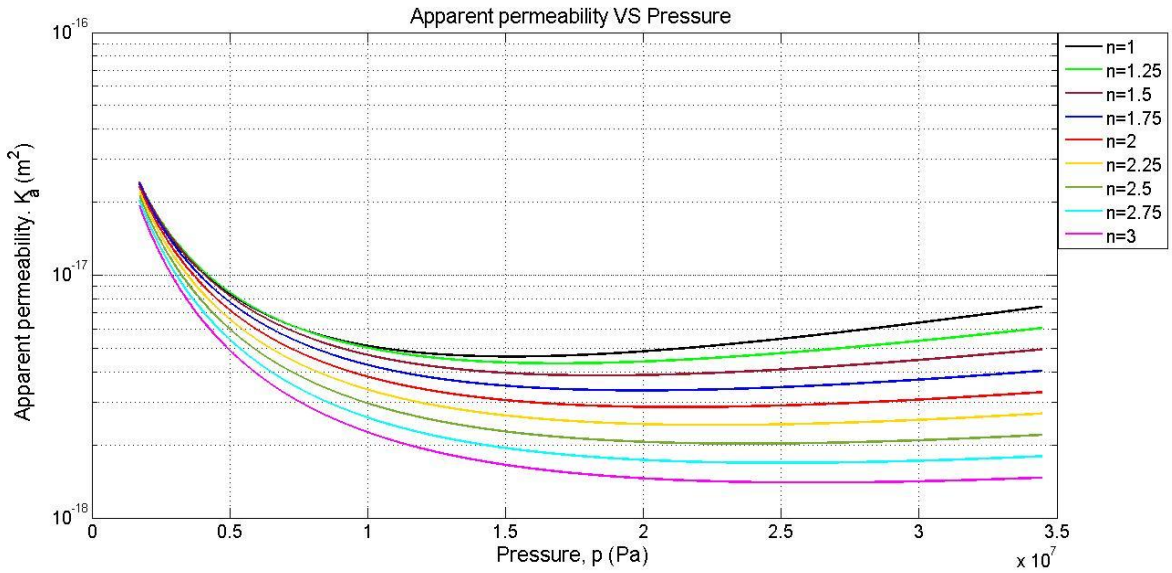

Figure 9 Apparent permeability as a function of pressure for different dimensional boundary of the pore spaces ($K_a(p)$ equation 2.48).

It is notable how apparent permeability changes when most of the pore shapes are fracture or cylinder pore styles (low n values). To understand this behavior it is necessary to see the dimensional boundary's effect on the pore radius because the pore radius appears in both free gas saturation relation and apparent permeability relation.

Extensive results carried out show that compressibility and desorption of gas have an essential role in our model. Since at low pressures both ΔR and R will decrease due to gas desorption and compaction effect respectively, it is interesting to see how the ratio of $\Delta R/R$ changes as a function of pressure for different values of n, and which one will dominate this change.

Figure 10, shows the change in the ratio of adsorption layer thickness to the pores' radius during the pressure reduction ($\Delta R/R$).

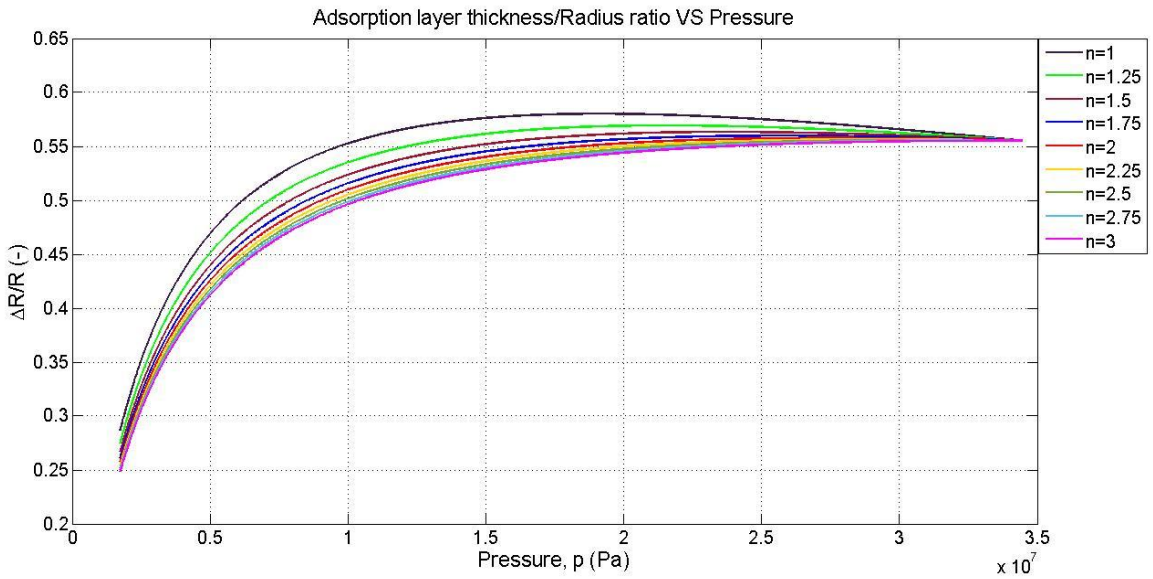

Figure 10 Ratio of adsorption layer thickness to the pore radius as a function of pressure ($\Delta R/R$ (p), equation 2.45 and 2.22) for different dimensional boundary of the pore spaces.

When pressure reduces during the production from shale reservoir, gas molecules desorb from the wall of the pores and adsorption layer thickness (ΔR) decreases. At the same time we can see from **Figure 5** that pressure decline leads to porosity decline, and due to relation 2.45, reduction of porosity is directly related to the reduction of the current radius of the pores. It is clear from **Figure 10** that at the beginning of pressure decline, radius decrease, is more dominant as we see a slight increase in $\Delta R/R$ ratio. This rise is even more in cases of low n values. If we look at equation 2.45, we can see that by decreasing n, we will increase the impact of porosity change (compaction effect) on pore radius (**Figure 11**). This is due to the unique arrangement and packing of the pore spaces, which can be affected significantly by compression of the shale matrix due to depletion.

We decided to use the value $\mathrm{n} = 2$ as a base case for the dynamic model to represent an average of all different pore shapes.

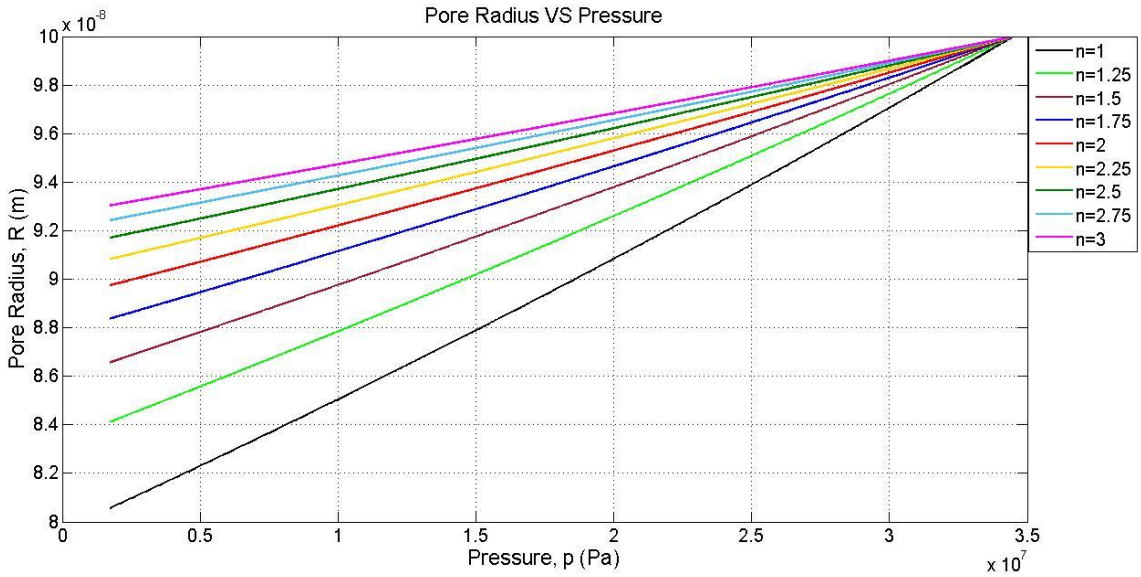

Figure 11 Pore radius as a function of pressure (R (p), equation 2.45) for different dimensional boundary (n) of the pore spaces.

Based on equation 2.45, **Figure 10** and **Figure 11**, we realize the importance of porosity and compaction effect on pore radius. However, we can have a better understanding by plotting the ratio of adsorption layer thickness to the radius of pores ($\Delta R/R$) during the pressure reduction for different compressibility values as shown in **Figure 12**.

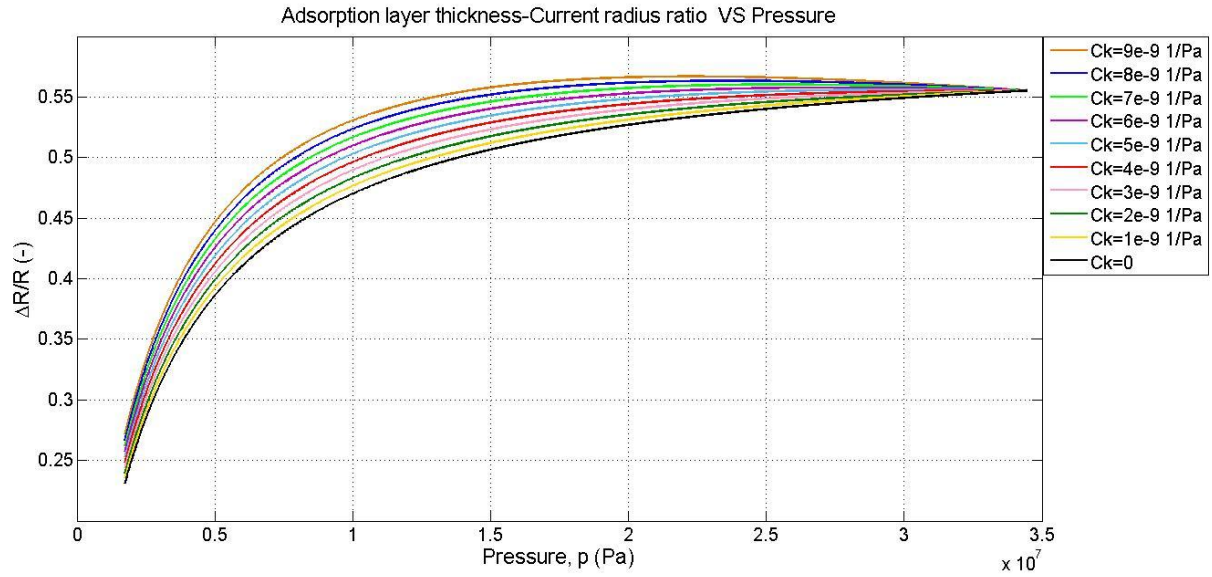

Figure 12 Ratio of adsorption layer thickness to the pore radius as a function of pressure ($\Delta R/R$ (p), equation 2.45 and 2.22) for different Compressibility values.

3.2.4. Role of Adsorption Layer Thickness and Initial Adsorbed Gas Fraction

One of the main goals of this study is to investigate the effect of the adsorption layer on reservoir properties and gas production. By "effect of adsorption layer" we mean the change in the thickness of the adsorption layer during production. When a shale gas reservoir is producing by the

mechanism of pressure drop, gas molecules that are adsorbed on the wall of pore spaces can desorb and join the free gas fraction inside the pore space and move toward the well. Meanwhile, the effective pore radius is also changing as a result of gas desorption. Additionally, the adsorbed layer thickness (ΔR) reduces as the gas molecules detach from the wall.

We can see from the literature that a value of 10 to 50nm (Kuila and Prasad 2011, Yu, Sepehrnoori et al. 2016, Lan, Moghanloo et al. 2017) is assigned to pore radius. Here in this study, we used a constant value of 100nm for the original pore radius ($R_0 = 100nm$) and a maximum adsorption layer thickness of 60nm ($\Delta R_{max} = 60nm$), which ultimately will give us a range of pore radius within real values ($R_{effective} = R - \Delta R$).

Before we study the evolution of adsorption layer thickness, we need to be confident that the initial state for the ratio of adsorbed gas to free gas saturation in our model is sustainable. For this purpose, it is beneficial to see the free gas and adsorbed gas mass at the initial condition. Based on mass conservation relation in our model (2.53), if necessary, we can adjust the amount of free and adsorbed gas initially in place by tuning adsorbed gas density or maximum adsorption layer thickness. **Figure 13** and **Figure 14** illustrate the adsorbed gas mass fraction in the reservoir at the initial condition and during the pressure reduction based on the mass conservation relation (2.53) in our model.

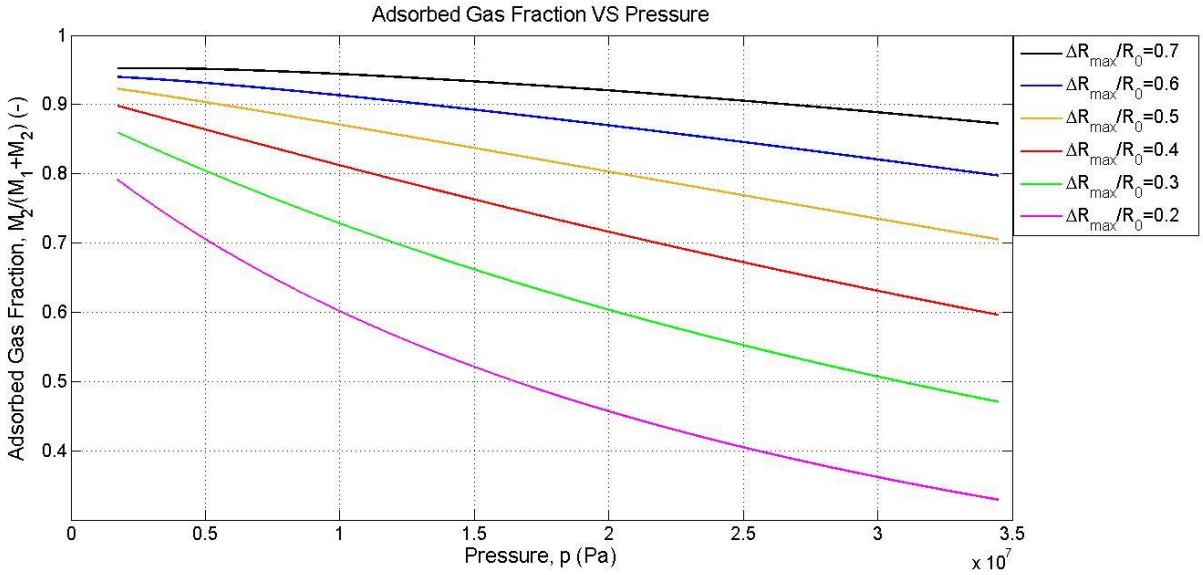

Figure 13 Adsorbed gas mass fraction as a function of pressure ($\frac{M_2}{M_1+M_2}(p)$ equation 2.72 and 2.73) for different "Maximum adsorption layer thickness-Original pore radius ratio ($\Delta R_{max}/R_0$)" and fixed Density of adsorbed gas.

Figure 13 shows the initial adsorbed gas mass fraction and how they change as a function of pressure based on 2.72 and 2.73 relations. The tuning property here is the value of ($\Delta R_{max}/R_0$) which is the ratio of "Maximum adsorption layer thickness to Original pore radius." As shown in **Figure 13**, for the high value of $\Delta R_{max}/R_0$ (=0.7) the adsorbed gas mass accounts for up to 87% of the total initial gas in place. In contrast, this ratio can decline down to 32% for low values of $\Delta R_{max}/R_0$ (=0.2). After a particular value $\Delta R_{max}/R_0$ (around 0.32), the initial free and adsorption gas in place have the same mass (it should be noted that all mass units are in the unit of pressure, see **Section 2.12**).

In **Figure 14**, we used adsorbed gas density as a tuning property to investigate the initial adsorbed gas fraction in place. In this figure, the value of $\Delta R_{max}/R_0$ is considered fixed (0.6) and we only changed the adsorbed gas density.

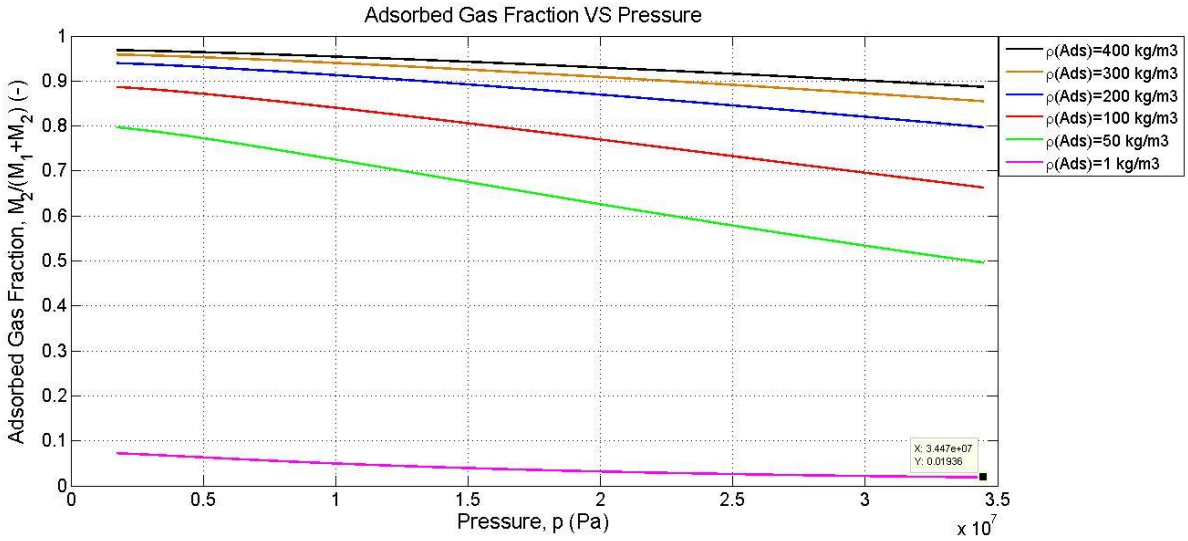

Figure 14 Adsorbed gas mass fraction as a function of pressure ($\frac{M_2}{M_1+M_2}(p)$ equation 2.72 and 2.73) for different "Density of adsorbed gas (ρ_a)" and fixed Maximum adsorption layer thickness.

Changing the adsorbed gas density will not affect the free gas mass curve. This can also be seen from the relation 2.72. On the other hand, increasing the adsorbed gas density can increase the amount of initial adsorbed gas in place. Liquid methane has a density of $420\ \mathrm{kg/m^3}$. If we consider the adsorbed gas layer as an extremely dense methane liquid, adsorbed gas mass can account for up to 88% of the total initial gas in place. If we use a meager value of $1\ \mathrm{kg/m^3}$ for adsorbed gas density (which is very close to the gas state of methane), only 2% of the total initial gas in place is consists of the adsorbed gas mass.

Choosing a very dense adsorbed gas density (liquid state of methane) may occupy tiny volumes and not impact the apparent permeability. **Figure 15** shows the behavior of apparent permeability as a function of pressure for different values of maximum adsorption layer thickness/Original pore radius ratio $\Delta R_{max}/R_0$.

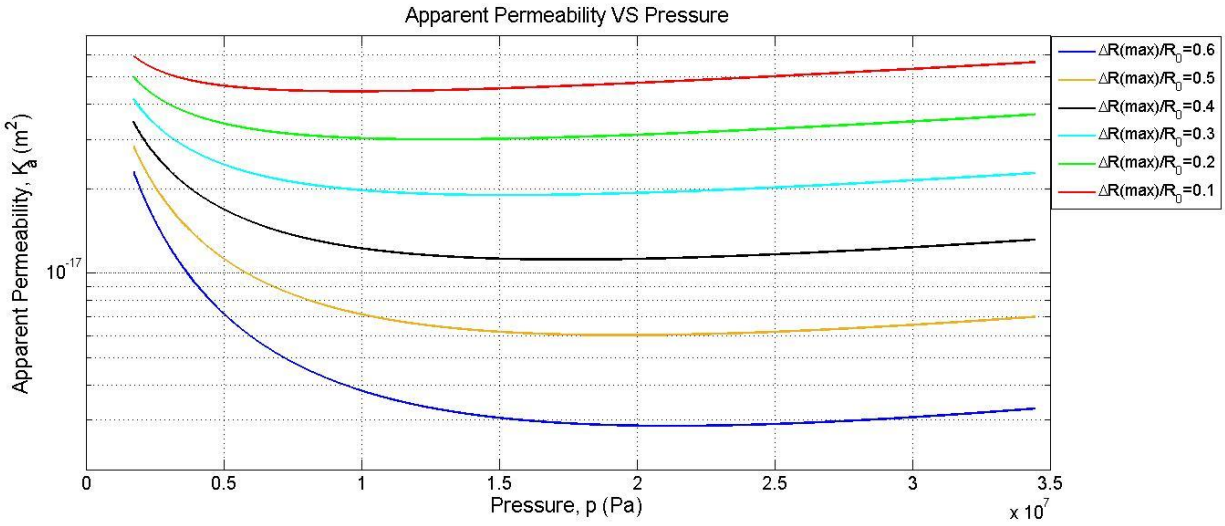

Figure 15 Apparent permeability as a function of pressure ($K_a(p)$ equation 2.48) for different "Maximum adsorption layer thickness-Original pore radius ratio ($\Delta R_{max}/R_0$)".

It is shown in **Figure 15** that small values of $\Delta R_{max}/R_0$, do not impact the apparent permeability during the pressure reduction.

Figure 16 shows the effect of different dimensional boundary (n) at fixed values of adsorbed gas density (=200 kg/m^3) and maximum adsorption layer thickness (=60 nm).

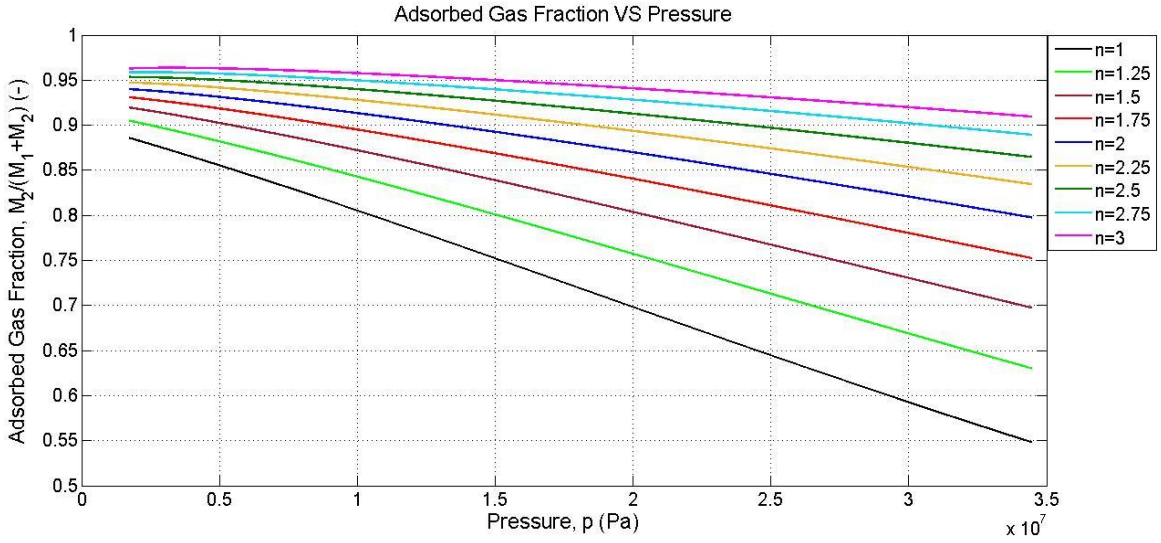

Figure 16 Adsorbed gas mass fraction as a function of pressure ($\frac{M_2}{M_1+M_2}(p)$ equation 2.72 and 2.73) for different "dimensional boundary of the pore spaces (n)" and fixed adsorbed gas density and Maximum adsorption layer thickness.

As we saw in **Figure 8**, by increasing the dimensional boundary values, free gas saturation decreases. **Figure 16** demonstrates the same result as the fraction of adsorbed gas increases by increasing the dimensional boundary. We get many different types of pore shapes inside the pore space in high values for the dimensional boundary. This is indicative of providing more inner surface area, and therefore gas molecules can sit on the wall of these pore spaces and result in a higher amount of adsorbed gas content.

From the results above and based on our model, we considered $\frac{\Delta R_{max}}{R_0} = 0.6$, $\rho_a = 200 kg/m^3$, and $n = 2$ as our base case scenario. **Figure 13**, **Figure 14**, and **Figure 16** show the dark blue line represents the adsorbed gas fraction. We considered $200 kg/m^3$ for adsorbed gas density because the adsorbed layer on the wall of pores inside the shale is not precisely a liquid form, but still, it is considered a very dense layer of gas molecules adsorbed on the organic matter.

These reference values will give us 79% of adsorbed gas fraction in the total gas initially in place. They will be considered as fixed values in the entire dynamic simulation in this study.

In line with the previous points mentioned above, it is beneficial to see the impact of the adsorption layer and compressibility on apparent permeability. Based on the relation 2.48, apparent permeability is related to absolute permeability and the Knudsen number. These parameters are a function of other parameters such as porosity, effective radius, free gas saturation, and pressure. It is interesting to see the relationship between some of these parameters to understand the model better.

Two cases are studied to quantify the net influence of gas desorption: (1) we will see the effect of changing in the thickness of adsorbed gas, this means both free and adsorbed gas is being produced during the production; and (2) where we consider a fixed gas adsorbed layer in the pores and only free gas is produced. The aim is to study the influence of gas desorption on gas pressure distribution and the evolution of apparent permeability. At the same time, we also want to know if compressibility plays a vital rule in production. Therefore, we considered two other cases where (3) the compaction effect is considered, and (4) there is zero compressibility.

Figure 17 shows the Knudsen number as a function of pressure. We can see from 2.49 that the effective radius influences the Knudsen number. The effective radius is also a function of adsorption layer thickness and pore radius ($R_{effective} = R - \Delta R$). In **Figure 17**, we can see four different cases where we studied the effect of producing gas from the adsorption layer and the effect of compressibility.

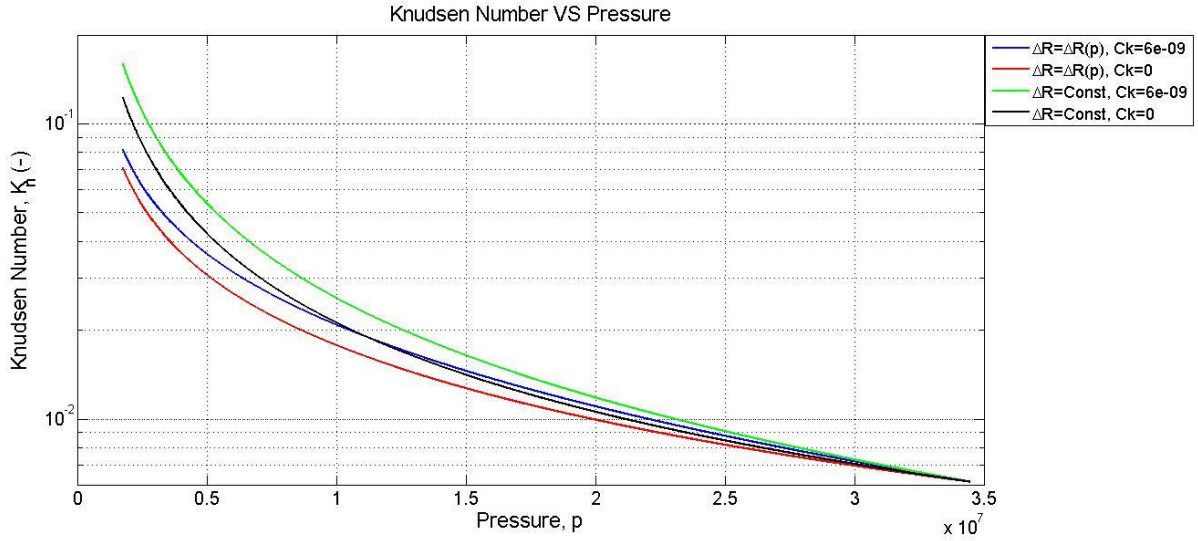

Figure 17 Effect of Adsorption layer and Compressibility on Knudsen number as a function of pressure ($K_n(p)$ equation 2.49).

From **Figure 17**, it is clear that the Knudsen number increases more in the case of no production from the adsorption layer compare to the other scenarios. When gas molecules desorb from the wall of pore spaces and join the free gas saturation, the number of molecules in the free gas space increases drastically. Consequently, the probability of collisions between gas molecules is much higher than collisions between the molecules and the pore walls, and gas transport is mainly governed by viscous flow. This results in a lower range of the Knudsen numbers (**Figure 4**).

Figure 17 also shows the effect of compaction. If we consider the compressibility, the pore space is under the effect of compaction, and as we saw in **Figure 11**, the pore radius becomes smaller. According to equation 2.49, the effective pore radius has an inverse relation with the Knudsen number, and it will result in higher values of the Knudsen number. Therefore, the case in which there is zero compressibility always has lower Knudsen number values than the cases with compaction effect.

Figure 18 shows the relation between apparent permeability and pressure. It shows that during the shale gas production and with the pressure dropping, apparent permeability increases significantly when there is gas production from the adsorption layer compare to cases where there is no production from the adsorbed layer.

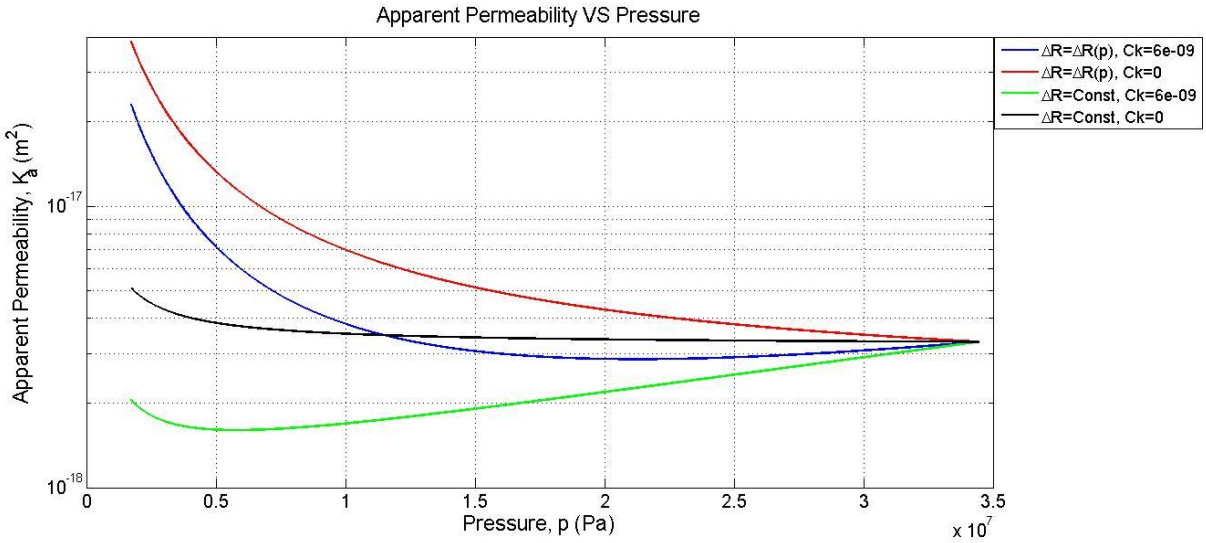

Figure 18 Effect of Adsorption layer and Compressibility on Apparent permeability as a function of pressure ($K_a(p)$ equation 2.48).

As was discussed in chapter 2, apparent permeability is a function of porosity, effective radius, free gas saturation, and the Knudsen number (2.48), the latter two are the function of effective radius and adsorption layer thickness themselves. As it is not generally clear what the relation of pore radius and apparent permeability will be, it is interesting to see the behavior of $\Delta R/R$ as a function of pressure for these 4 cases (**Figure 19**).

To study the effect of compressibility on apparent permeability, we considered different cases where we simply assume zero compressibility (no change in porosity) with and without adsorption effect (production of adsorbed gas). If we look at the trends during the pressure reduction, we can see that the apparent permeability uptake increases dramatically in the scenarios when we consider adsorbed gas production. In contrast, the compaction effect's presence seems to have a negative

effect on apparent permeability as they reduce the pore throat size. We can clearly see the effect of compaction on pore radii in **Figure 19**, where we get high ratios of $\Delta R/R$ as a result of the reduction in pore radius (R).

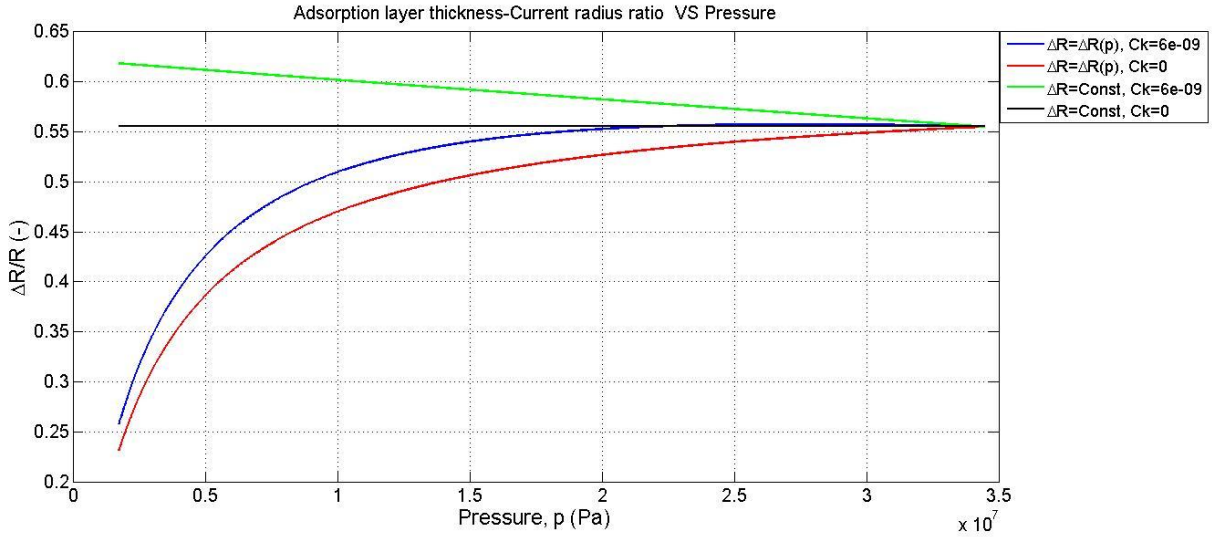

Figure 19 Effect of Adsorption layer and Compressibility on the Ratio of adsorption layer thickness to the pore radius as a function of pressure ($\Delta R/R$ (p), equation 2.45 and 2.22)

It is essential to highlight how production from the adsorption layer becomes dominant in low-pressure ranges. As we can see from **Figure 19**, the green line (Case with only considering the compaction effect) shows a linear change during the entire pressure drop period while the red line (Case with only considering the changing in the adsorption layer thickness) shows a non-linear decline, especially at low pressures.

As shown in **Figure 18** the effect of adsorption layer thickness is significant for apparent permeability. This is mainly because of the vital rule of the effective radius concerning 2.48, 2.49, and 2.50.

These results now provide evidence of the importance of considering compressibility and production from the adsorption layer, leading to a change in the size of pore radii inside the shale matrix.

To clarify the relation between apparent permeability and the Knudsen number, it is beneficial to demonstrate how they are related to each other. **Figure 20** illustrates the apparent permeability profile as a function of the Knudsen number.

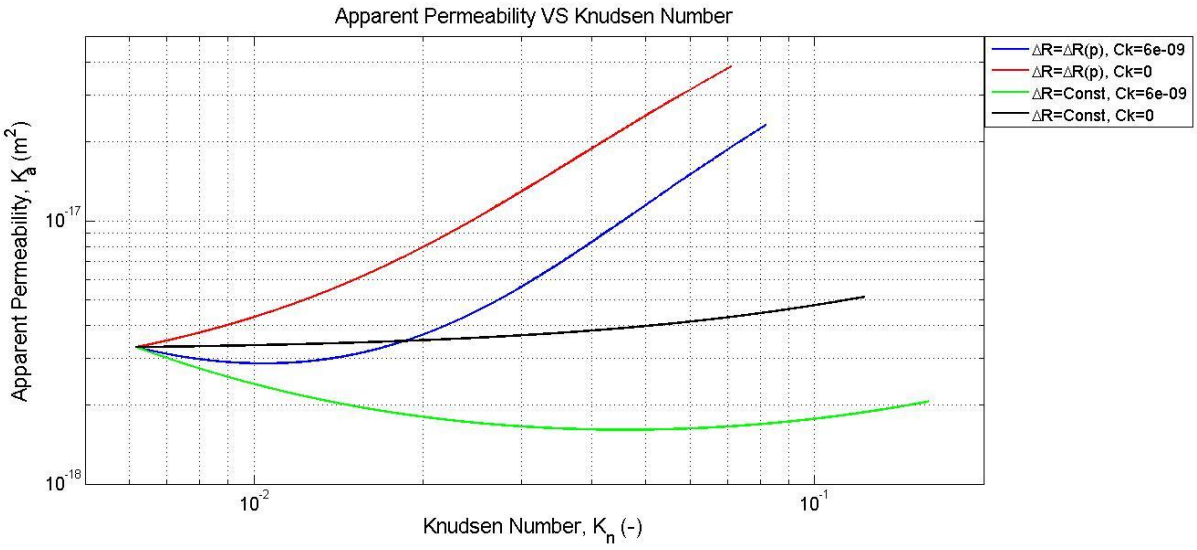

Figure 20 Effect of Adsorption layer and Compressibility on Apparent permeability as a function of Knudsen number ($K_a(K_n)$ equation 2.48).

If we compare the result from **Figure 19** with **Figure 20**, we realize the importance of an effective radius in our model. In the case when there is no production from adsorbed gas in the pores, and the compaction effect reduces the pore radius, we can see that even though, the Knudsen number is increasing significantly, the apparent permeability is yet decreasing. This is because of the increase in the ratio of $\Delta R/R$ (**Figure 19**), which means that the effective radius is decreasing, and it has a vital impact on apparent permeability.

3.3. Dynamic Simulation Results

In this section, we study the dynamic interplay of all properties that we studied in the previous section using simulations at the core scale. An original pore radius of 100nm is assumed for a 20m core. The input parameters listed in **Table 1** are applied.

Based on the model's behavior in the previous section, the values in **Table 2**, were considered a base case in our study and will be constant during the entire simulation. **Table 2** also indicates the input data regarding to the core sample and time steps.

Table 2 Input parameters that are considered constant during the simulations.

Parameters	Value	Units
Total compressibility factor, C_k	$6 * 10^{-9}$	$1/\text{Pa}$
Matrix initial porosity, ϕ	0.1	–
Dimensional boundary, n	2	–
Maximum adsorption layer thickness, ΔR_{max}	60	nm
Adsorbed gas density, ρ_a	200	kg/m^3
Number of Grid Cells, N_x	20	-
Number of Time Steps*	15000	
Total time of the simulation, T_{total}	1000	days

*The full explanation of acquiring suitable number of steps can be found in **C**

As we start production from the core sample at $t = 0$, reservoir pressure ($p = P_{init}$) starts to decline until it gets to well pressure. **Figure 21** illustrates the evolution of the recovery factor and pressure over 1000 days of production for four different cases where we investigate the presence

and absence of compaction effect and the effect of production from the adsorption gas layer (changing in the thickness of the adsorbed gas layer compare to when the thickness of the adsorbed gas layer is constant). We chose 1000 days as the total production time to achieve a stabilized recovery factor evolution at the final stages of recovery in our base case. This also means that the pressure evolution becomes stable and reaches the well pressure value. It should be noted that the values for pressure address the average values alongside the core sample (the averaging methods were discussed in **Section 2.13**).

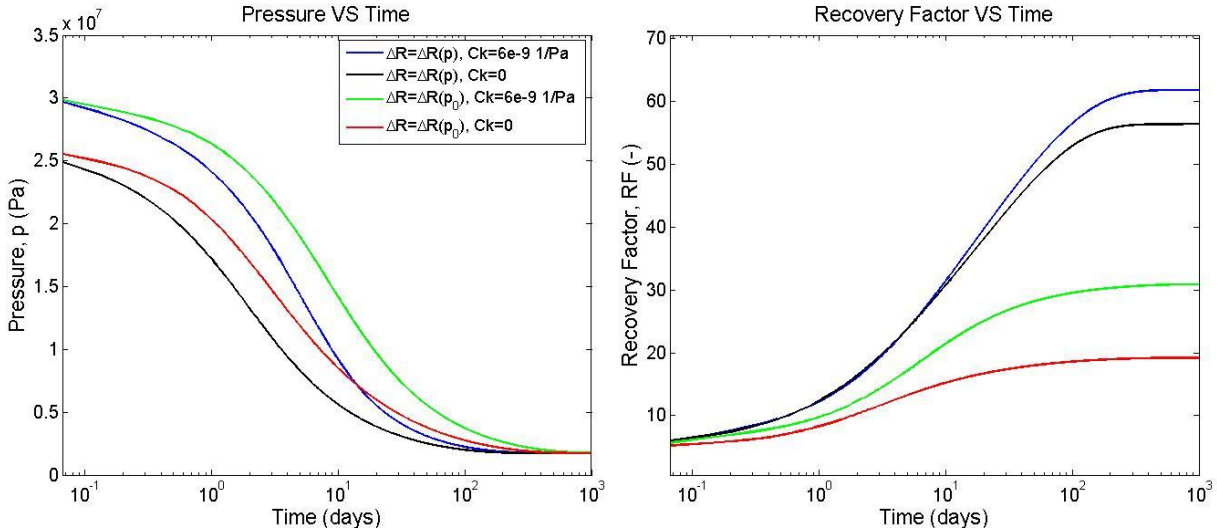

Figure 21 Left Side: Reservoir pressure (Average pressure alongside the core) VS time ($p\ vs\ T_{total}$), Right Side: Recovery Factor VS time ($RF\ vs\ T_{total}$).

Figure 21 highlights the importance of considering both the compaction effect and adsorbed gas production effect during shale gas production, the more detailed investigation on each effect will be discussed in the following of this section. As we can see, even though the initial pressure of the reservoir and the abandonment well pressure of different scenarios are the same (all initial pressures are equal to initial pressure value ($3.447 * 10^7$) which cannot be seen at the starting point ($time = 0$) due to use of Log scale on the x-axis.), our base case scenario (Blue curve) delivers a significantly higher recovery factor (61.82%) compare to other scenarios. A further finding is that the effect of adsorbed gas production and the reducing adsorption layer thickness has more influence on recovery than the compaction effect. The recovery factor for the case when we only consider the effect of adsorbed gas production (Black curve) is 56.37%, while it reduces to 30.91% for the case when we only consider the compaction effect (Green curve). However, this does not vanish the influence of the compaction effect as neglecting the compressibility of the shale play as the remaining effect (Red curve), and just considering the production from the free gas inside the matrix can reduce the recovery to 19.2%.

3.3.1. Role of Compressibility

We studied the effect of compressibility in **Section 3.2.1** Here we want to investigate how different compressibility values can affect the performance of a shale play. **Figure 22** shows the effect of different compressibility values in the production of shale gas by illustrating pressure (average pressure) and recovery factor profiles over 1000 days.

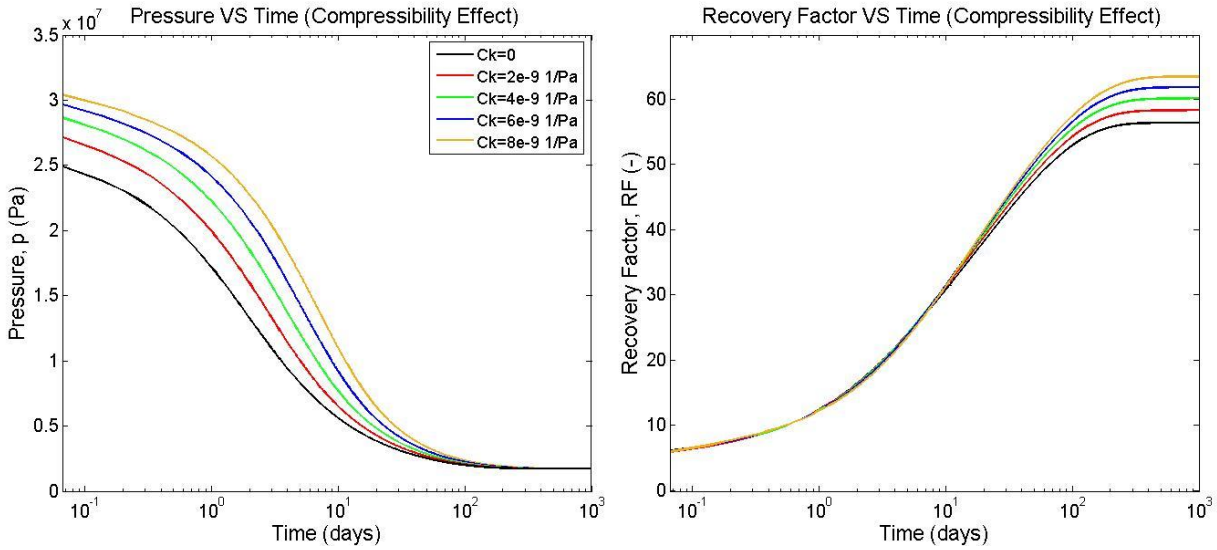

Figure 22 The effect of Compressibility on reservoir performance. Left Side: Reservoir pressure (Average pressure alongside the core) VS time ($p\ vs\ T_{total}$), Right Side: Recovery Factor VS time ($RF\ vs\ T_{total}$).

As we can see from Figure 21, higher compressibility values result in higher recovery due to compressing the matrix. It should be noted again that in the pressure profiles (Left side) all starting points are the same initial pressure value ($3.447 * 10^7$) which cannot be shown at the starting point ($time = 0$) due to use of Log scale on the x-axis.

The results from solving the mass conservation equation (2.53) provide a new value for pressure at each time step, and we can update all of the properties of the shale reservoir at each time step. We update each property in a single cell of the core sample. To plot each property's evolution over time, we need to use the averaging methods in **Section 2.13**, and this will help us achieve a unique value of the property at each time step along with the entire core sample.

For a better understanding of compressibility effect on some of reservoir properties, simulation results using average property calculations are shown in **Figure 23**. In this figure, we can observe the evolution of Porosity, Free gas saturation, $\Delta R/R$ ratio, and Apparent permeability over time along the core length and see the effect of compressibility on these properties.

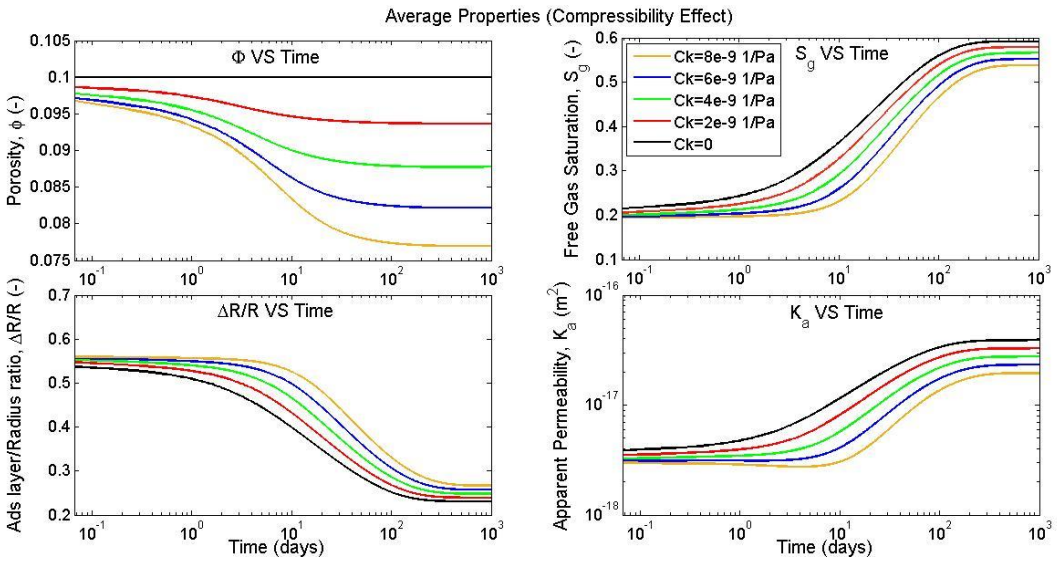

Figure 23 Dynamic simulation results for four different average properties over time to study the effect of Compressibility. Top left:ϕ vs T_{total}, Top right: S_g vs T_{total}, Bottom left:$\Delta R/R$ vs T_{total}, Bottom right:K_a vs T_{total}.

Properties vary over time in the same scope as the results from the static model, however, because in the static model section we used a linear change in pressure values, here, by observing the dynamic simulation results, we can have a better understanding of how different properties change over the production lifetime as we update the pressure values at each time step using discretization (**Section 2.10**).

We can see the effect of increasing the compressibility in all four plots. As we increase the value of compressibility, the porosity declines to a greater extend during the production (Top left), higher compressibility also means smaller effective radius as the pores will compress more and therefore we see higher values for $\Delta R/R$ ratio. According to equation 2.47 higher ratios of adsorption layer thickness to radius ($\Delta R/R$) results in lower free gas saturation, and eventually lower values for apparent permeability. Higher compressibility means that the porosity is lower at a given pressure, and more gas is produced. The density of gas is still the same at that pressure, but it has less space. The adsorption layer thickness is the same at this pressure but the volume is lower since it is a layer on a smaller radius. The permeability does not affect the ultimate value of the end recovery, it only controls how fast to reach it.

These results verify the fact that higher values of compressibility lead to higher recovery factor due to compressing the matrix and producing more of the free gas (Higher recovery factor in **Figure 21**).

One concern about using the averaging method is that each property has a different value at each cell of the core sample at a different time step, and the difference between the values can be considerable at some stages during the dynamic simulation. To have a more thorough investigation of properties changes over time, we used distribution graphs. Distribution graphs show each property's real unique value at all 20 cells of the core sample at a specific time step. We chose five specific time step to draw the distribution graphs; these time steps are as follow:

- Beginning of the production.
- When production reaches 25% of Ultimate recovery ($RF_{frac} = 25\%$).

- When production reaches 50% of Ultimate recovery ($RF_{frac} = 50\%$).
- When production reaches 75% of Ultimate recovery ($RF_{frac} = 75\%$).
- End of the production.

We looked for the times that each of these fraction of ultimate recovery factors is achieved, and based on 1000 days of production in the dynamic simulation of our base case model with the recovery of 61.82%, we obtained the following results.

- $RF_{frac} = 25\%$ happens at $Time = 1.87\ days$
- $RF_{frac} = 50\%$ happens at $Time = 9.6\ days$
- $RF_{frac} = 25\%$ happens at $Time = 35.53\ days$

Figure 24 to **26** show distributions of different properties at the 5 times mentioned above.

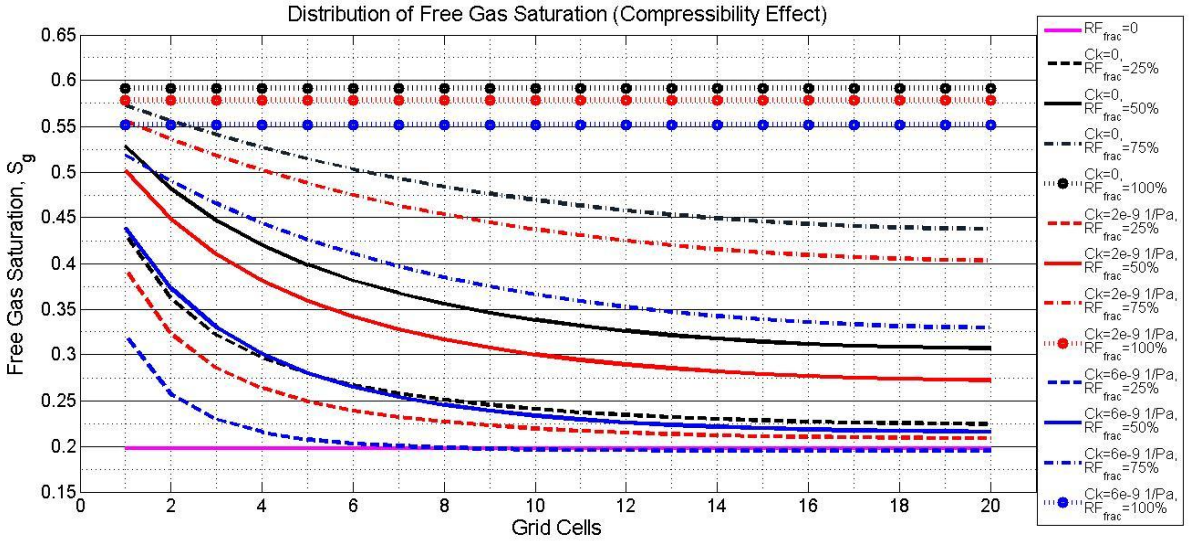

Figure 24 Distribution of Free gas saturation (S_g) at different "Fraction of ultimate recovery factors (RF_{frac})" for different Compressibility (C_k)

All cases have the same initial property distribution at the beginning of the production (Pink line). The distribution curves in **Figure 24** indicates that due to producing the gas from the left side of the core, the effect of each property (in this case, free gas saturation) starts from the starting cells first and then propagate through the entire core sample gradually. Each property's influence will continue until we reach the well pressure, and they will all stabilize at the end of production (Dot lines).

Figure 24 also verifies that higher compressibility results in lower free gas saturation at any time of the production as we are producing more gas from the core (Higher recovery in **Figure 22**). It can be seen that at each individual time, the distribution of each property is minimum for the case with the highest compressibility (Blue curves).

Figure 25, Figure 26 and **Figure** 27 show the distribution of Porosity, $\Delta R/R$ ratio and Apparent permeability respectively.

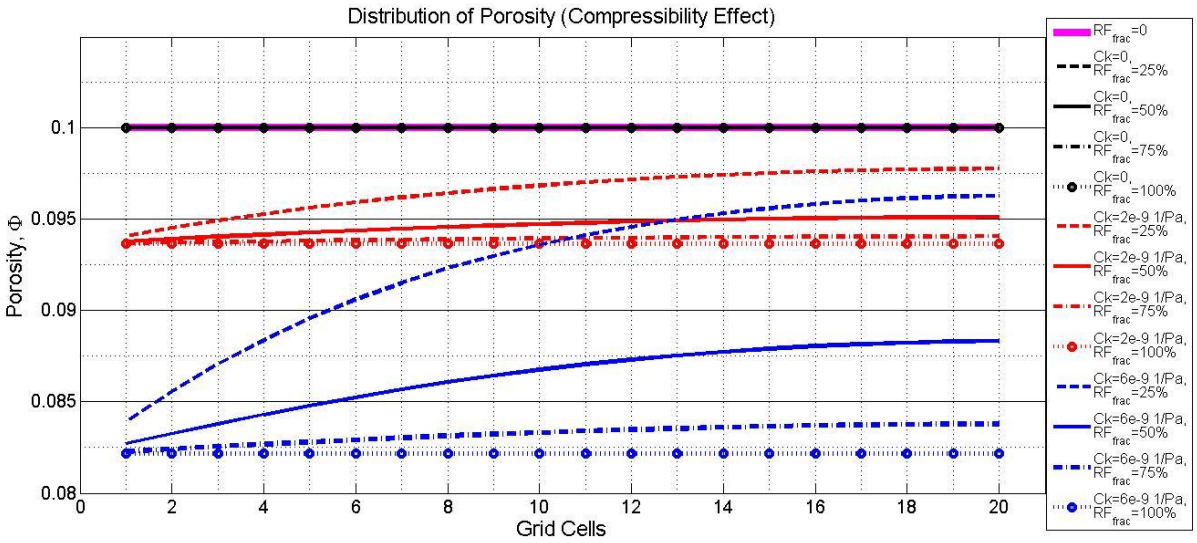

Figure 25 Distribution of porosity (ϕ) at different "Fraction of ultimate recovery factors (RF_{frac})" for different Compressibility (C_k)

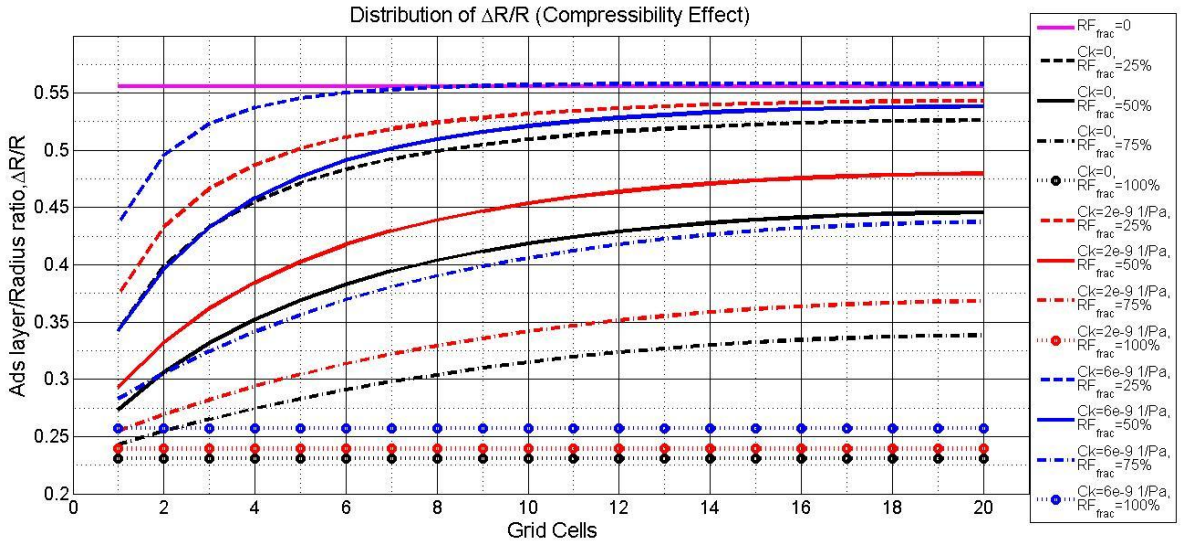

Figure 26 Distribution of $\Delta R/R$ at different "Fraction of ultimate recovery factors (RF_{frac})" for different Compressibility (C_k)

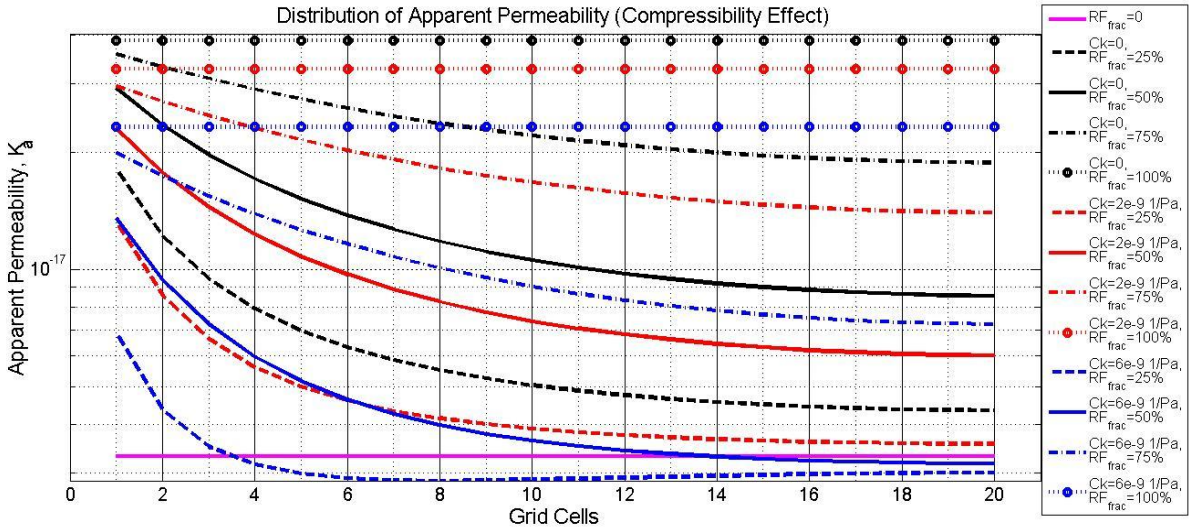

Figure 27 Distribution of Apparent permeability (K_a) at different "Fraction of ultimate recovery factors (RF_{frac})" for different Compressibility (C_k)

At the initial condition, before producing the gas from the shale matrix ($RF_{frac} = 0$, Pink curve), we have a continuous line for all cases in **Figure 24-Figure** 27. When we start producing, we can see that the effect of pressure reduction first reaches the starting grid cells, and it takes time until it uniformly reaches the other end of the matrix.

In **Figure 25**, when compressibility is zero (Black curves), there is no change in distribution lines during the production, and as we saw from **Figure 5**, higher values of compressibility result in lower porosity values at the end of production. This result verifies that higher compressible reservoirs can be compressed more during depletion and reach higher recovery factors.

Because compressing the matrix can decrease the pore radius (R), but it does not affect the adsorption layer thickness (ΔR) (2.45 and 2.52 Figure 7 and **Figure 12**), we can see in **Figure 26** that the ratio of adsorption layer thickness to pore radius ($\Delta R/R$) reduces less, compare to the case with zero compressibility (it has a higher value at the end).

Finally, for the more compressible case (our base case), the lower free gas saturation, lower porosity and higher $\Delta R/R$ (which means lower effective radius ($R - \Delta R$)), all results in lower apparent permeability as can be seen in **Figure 27**, which once again verifies the higher recovery due to depleted adsorbed and free gas.

The results of distribution graphs provides evidence that the use of averaging methods for different properties was accurate enough to analyze the behavior of each matrix property over the production time.

3.3.2. Role of N-Sphere Geometry or Dimensional Boundary

In **Section 3.23.2.3**, we saw the static effect of the dimensional boundary (n) on free gas saturation, pore radius, and apparent permeability. We studied how the n-sphere different geometry can affect different properties. In **Figure 287**, we can observe the effect of dimensional boundary (n) on the recovery factor and pressure profile.

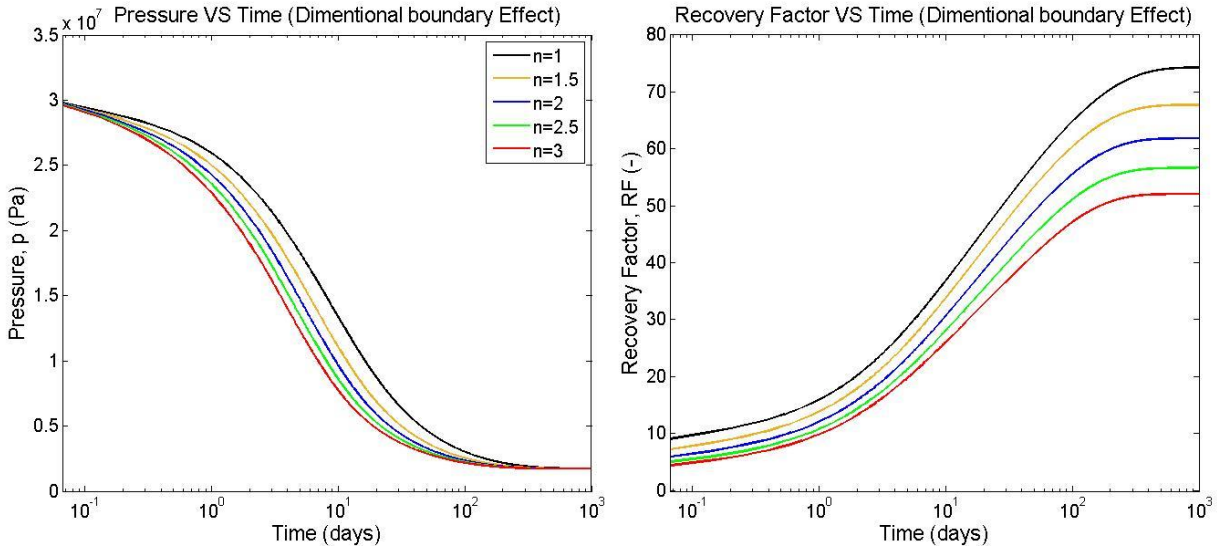

Figure 28 The effect of Dimensional boundary (n) on reservoir performance. Left Side: Reservoir pressure (Average pressure alongside the core) VS time (p vs T_{total}), Right Side: Recovery Factor VS time (RF vs T_{total}).

Figure 28 illustrates how n-sphere pore geometry can affect the pressure and recovery factor evolution during the reservoir depletion. As we saw in **Section 3.23.2.3**, decreasing the n value means that the pore space's geometry is more similar to fracture geometry, and we saw a higher value of free gas saturation and apparent permeability. As shown in the recovery factor curves, the highest amount of recovery after 1000 days (74.28%) belongs to the case when we consider the dimensional boundary equal to 1. In contrast, for pore geometries of higher dimensions ($n = 3$), the recovery factor decreases to 52.05% .

To investigate different properties evolution over time, **Figure 29** provides simulation results for average properties during the gas production from the shale matrix.

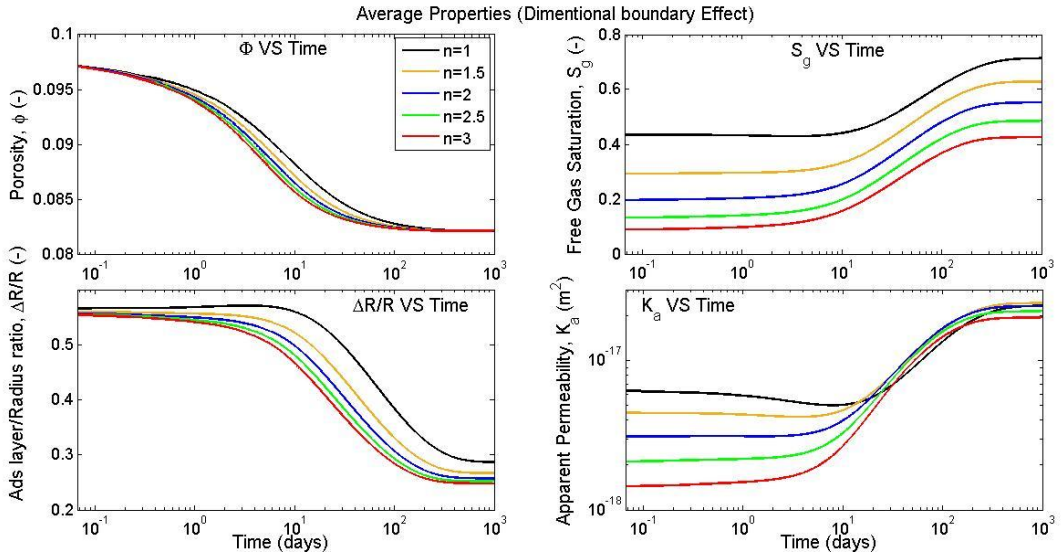

Figure 29 Dynamic simulation results for four different average properties over time to study the effect of Dimensional boundary (n). Top left:ϕ vs T_{total}, Top right: S_g vs T_{total}, Bottom left:$\Delta R/R$ vs T_{total}, Bottom right:K_a vs T_{total}.

It is important to notice how apparent permeability curve changes for the case when n equals to 1. As we mentioned before, n equals to 1, means that the pore shape geometry looks like a fracture. From equation 2.47 and **Figure 8**, it is clear that with smaller values for n, we have a higher amount of free gas saturation inside the pores, and this is also verified by **Figure 29** top right figure. On the other hand, due to relation 2.45 and **Figure 11**, pore radius decreases significantly for the cases with small values of n, and as we can see, the ratio of $\Delta R/R$ becomes higher for small values of dimensional boundary, this means the effective radius is smaller $(R - \Delta R)$. It can be concluded that the influence of the effective radius becomes more dominant than free gas saturation on apparent permeability evolution.

3.3.3. Role of Adsorption Layer Thickness and Initial Adsorbed Gas Fraction

Figure 13 in **Section 3.23.2.4**, demonstrates how the maximum adsorption layer thickness influences the adsorbed gas fraction at initial condition inside the reservoir. Here, we want to investigate the effect of maximum adsorption layer thickness on the recovery factor for three different cases when; (a) adsorbed gas fraction is higher than a free gas fraction, (b) adsorbed gas fraction is equal to free gas fraction and (c) adsorbed gas fraction is lower than a free gas fraction. **Figure 30** delivers the results of this comparison. We chose three cases where initial adsorbed gas fraction accounts for 25% (Black curve), 50% (Red curve), and 75% (Green curve) of original gas in place (OGIP), respectively.

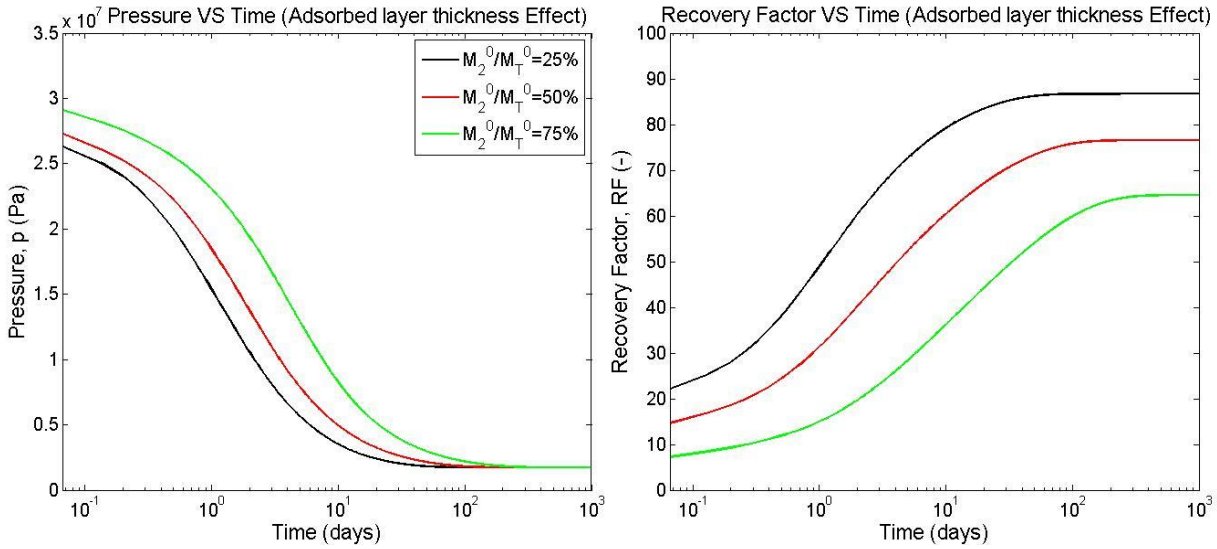

Figure 30 The effect of Adsorbed layer thickness (ΔR_{max}) on reservoir performance. Left Side: Reservoir pressure (Average pressure alongside the core) VS time (p vs T_{total}), Right Side: Recovery Factor VS time (RF vs T_{total}).

The initial adsorbed gas fraction is related to the maximum adsorption layer thickness (ΔR_{max}). Based on relation 2.72 and 2.73, mass fractions are a function of free gas saturation, which is directly related to the maximum adsorption layer thickness (ΔR_{max}). This relationship was investigated in **Figure 13**.

We are investigating the initial adsorbed layer thickness by changing the adsorbed mass fraction at the initial condition. For instance, the fractions that we investigated in **Figure 30**, each represent a different maximum adsorption layer thicknesses. These values are as follow

- We calculated 25% for Adsorbed mass fraction (M_2/M_{total}) when we set ΔR_{max} equal to

15.53nm

- We calculated 50% for Adsorbed mass fraction (M_2/M_{total}) when we set ΔR_{max} equal to 32.5nm
- We calculated 75% for Adsorbed mass fraction (M_2/M_{total}) when we set ΔR_{max} equal to 54.61nm

It is vital to mention that all three cases above have the same OGIP (Original Gas in Place) values, making them comparable. Our base case scenario with a maximum adsorption layer thickness of 60nm is very similar to the third case (Green curve), with 79% of the adsorbed gas fraction.

Simulation results in **Figure 30** demonstrate that the highest recovery factor is achievable when we have the least adsorbed gas fraction in the reservoir, and most of the shale gas is in the form of free gas (Black curve).

The results also reveal that the pressure profile stabilizes faster in the case of the least adsorbed gas fraction. On the other hand, when we have a high fraction of adsorbed gas at the initial condition, it takes a significantly longer time for pressure and recovery factor evolution to reach stabilization. This late stabilization is due to the gas production from the adsorbed layer until the end of the production period. This exciting finding can be better interpreted by plotting the mass fractions separately. **Figure 31** shows adsorbed and free gas masses in place profiles during the production for the same three cases, as in **Figure 30**.

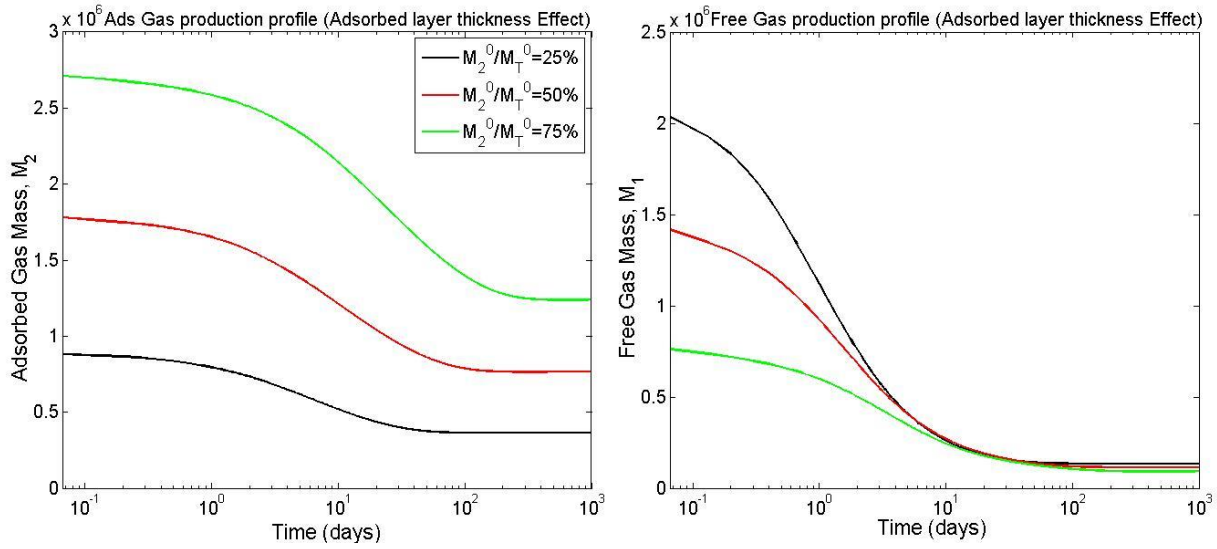

Figure 31 The effect of Adsorbed layer thickness (ΔR_{max}) on gas production performance. Left Side: Adsorbed gas in place VS time (M_2 vs T_{total}), Right Side: Free gas in place VS time (M_1 vs T_{total}).

From **Figure 31** (Left side), it is clear from the green curve that the adsorbed gas is being produced until the final stages of production. The adsorbed gas first desorbs from the wall inside the pores, then, joins the free gas fraction and finally it is produced alongside the already free gas in place. As a result we still can see a decline in free gas in place curve (Green curve, Right side) at the final stages of production, this is because adsorbed gas molecules are still detaching from the matrix and being produced. On the other hand the production of adsorbed gas stabilizes at early stages of production when we have only 25% of adsorbed gas fraction (Black curve, Left side). This also results in early stabilization of free gas in place (Black curve, Right side).

In the adsorbed gas in place profile (Left side), we can see that for the case with a high initial adsorption layer thickness, a significant amount of adsorbed gas is remaining inside the pores, which indicates the reason for the lower recovery of this case.

Figure 32 demonstrates the effect of different initial thicknesses of the adsorption layer on four average properties, using the model's dynamic simulation.

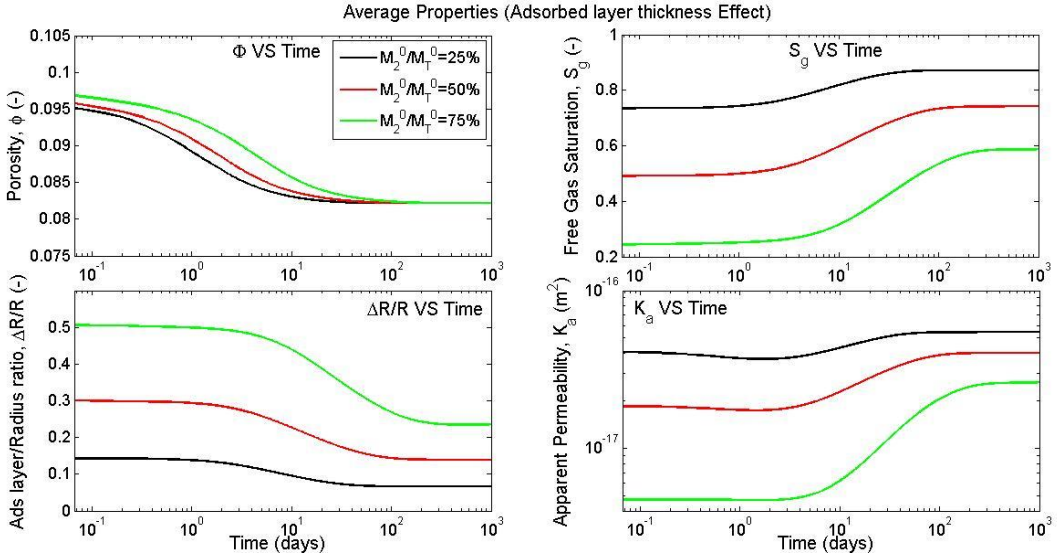

Figure 32 Dynamic simulation results for four different average properties over time to study the effect of Adsorption layer thickness (ΔR_{max}). Top left:ϕ vs T_{total}, Top right: S_g vs T_{total}, Bottom left:$\Delta R/R$ vs T_{total}, Bottom right:K_a vs T_{total}.

The results show that when we have the least adsorption layer thickness inside the pores (Black curves), we have a higher free gas saturation (Top right) because the ratio of adsorption layer thickness to the pore radius ($\Delta R/R$) is minimum (Bottom left). Simultaneously, with lower adsorption layer thickness, the effective radius is higher since most of the pore space belongs to free gas fraction, and therefore, apparent permeability will be higher.

One interesting trend in **Figure 32** is for the case, with an adsorbed gas fraction of 75%. In this case, we can see a high ratio of adsorption layer thickness to pore radius at the start of production. While producing a free gas from the pore space, the compaction effect reduces the pore space at the same time with desorbing gas molecules from the adsorption layer. This results in a steady profile in $\Delta R/R$ at the beginning of the production. However, we can see that the adsorption layer reduction becomes dominant very quickly, and we see a drastic decline in the $\Delta R/R$ profile, which consequently results in a sudden increase of apparent permeability over the same period.

4. Conclusion

Gas is stored in shale gas in the form of free and adsorbed gas inside the pores. In this study, we have investigated a new mathematical model for shale gas production by considering a compressible shale matrix which produces both free and adsorbed gas fractions. The role of geometrical and intrinsic properties of the matrix were investigated under static and dynamic conditions. The model is based on the assumption of an n-sphere pore geometry with a fixed solid volume. The goal was to consider and investigate the effect of compressibility of the matrix, the n-sphere pore geometry, and different characteristics of adsorbed gas inside the pore space such as the adsorption layer thickness, the adsorbed gas density and the initial fraction of adsorbed and free gas inside the pores. This study contains the investigation of many different aspects of shale gas production which can be studied individually or simultaneously.

Achieving our goals in this study here are the most important findings:

- The shale matrix's compressibility plays a vital role in gas production as it can affect the porosity to a great extent and compress the pore space as we produce. More compressible shales can be compressed more and more gas is extracted from them (Higher recovery).
- Even though compressing the matrix does not affect the adsorbed layer thickness (ΔR), it reduces the pore radius (R). Therefore, more compressible shales have smaller effective pore radiuses ($R - \Delta R$).
- Apparent permeability is a function of porosity, effective radius, free gas saturation, and the Knudsen number. The effective radius is the most effective property on apparent permeability; therefore, a smaller effective radius can significantly decrease apparent permeability.
- The n-sphere pore geometry is a good representative for the pore shapes inside the shale matrix. Small values of n, which represent fracture type shapes ($n = 1$), have bigger pore radii and higher free gas saturations. High values of n, which represent spherical pore shapes ($n = 3$), have smaller pore radii and lower free gas saturations. The pore geometry inside the shale is very complex; therefore, higher dimensions can also be considered. Also, n can be any real number as we have a mixture of different pore shapes inside the shale.
- Producing from the shale matrix results in desorbing gas molecules from the inside wall of the pore spaces. It is vital to consider decreasing adsorption layer thickness as it affects the recovery factor more than the compressibility effect.
- The initial adsorption layer thickness defines the adsorbed and free gas fraction inside the pore space. Thin layer of initial adsorbed gas inside the pore is equal to having more free gas saturation which means a significantly higher recovery.
- The ultimate free gas in place is independent of how thick the adsorption layer is at the initial condition. However, the amount of adsorbed gas that remains inside the pore space is directly related to the initial adsorption layer thickness and can define the recovery factor's difference.
- Even though both pore radius (R) and adsorption layer thickness (ΔR) are reducing during the production, the decrease rate of adsorption layer thickness (ΔR) always becomes dominant after a period, and this results in increasing the effective radius (or decreasing the $\Delta R/R$ ratio).

References

Agista, M. N., et al. (2019). "Modelling nanofluid injection in porous media." Journal of Petroleum Science and Engineering **176**: 836-849.

Akkutlu, I. Y. and E. Fathi (2012). "Multiscale gas transport in shales with local kerogen heterogeneities." SPE journal **17**(04): 1,002-001,011.

Andersen, P., et al. (2014). "A model for spontaneous imbibition as a mechanism for oil recovery in fractured reservoirs." Transport in porous media **101**(2): 299-331.

Anderson, J. M., et al. (2014). "Isothermal mass flow measurements in microfabricated rectangular channels over a very wide knudsen range." Journal of Micromechanics and Microengineering **24**(5): 055013.

Berawala, D. S. and P. Østebø Andersen (2019). Evaluation of Multicomponent Adsorption Kinetics for CO2 Enhanced Gas Recovery from Tight Shales. SPE Europec featured at 81st EAGE Conference and Exhibition, Society of Petroleum Engineers.

Beskok, A. and G. E. Karniadakis (1999). "Report: a model for flows in channels, pipes, and ducts at micro and nano scales." Microscale Thermophysical Engineering **3**(1): 43-77.

Bird, G. A. and J. Brady (1994). Molecular gas dynamics and the direct simulation of gas flows, Clarendon press Oxford.

Blum, J. (2019). Has the peak of the shale revolution come and gone?

Bustin, R. M., et al. (2008). Impact of shale properties on pore structure and storage characteristics. SPE shale gas production conference, Society of Petroleum Engineers.

Carman, P. C. (1956). "Flow of gases through porous media."

Chalmers, G. R. and R. M. Bustin (2007). "The organic matter distribution and methane capacity of the Lower Cretaceous strata of Northeastern British Columbia, Canada." International Journal of Coal Geology **70**(1-3): 223-239.

Chen, X., et al. (2008). "Nanoscale fluid transport: size and rate effects." Nano letters **8**(9): 2988-2992.

Cipolla, C. L., et al. (2010). "Reservoir modeling in shale-gas reservoirs." SPE reservoir evaluation & engineering **13**(04): 638-653.

Civan, F. (2007). Reservoir Formation Damage-Fundamentals, Modeling, Assessment, and Mitigation, Gulf Professional Pub, Elsevier, Burlington, MA.

Civan, F. (2010). "Effective correlation of apparent gas permeability in tight porous media." Transport in porous media **82**(2): 375-384.

Civan, F., et al. (2011). "Shale-gas permeability and diffusivity inferred by improved formulation of relevant retention and transport mechanisms." Transport in porous media **86**(3): 925-944.

Clarkson, C. R., et al. (2012). "Production analysis of tight-gas and shale-gas reservoirs using the dynamic-slippage concept." SPE journal **17**(01): 230-242.

Davudov, D. and R. G. Moghanloo (2018). "Impact of pore compressibility and connectivity loss on shale permeability." International Journal of Coal Geology **187**: 98-113.

Evans, H. (1947). "Volume of an n-dimensional sphere." The American Mathematical Monthly **54**(10): 592-594.

Fjar, E., et al. (2008). Petroleum related rock mechanics, Elsevier.

Florence, F. A., et al. (2007). Improved permeability prediction relations for low permeability sands. Rocky mountain oil & gas technology symposium, Society of Petroleum Engineers.

Freeman, C., et al. (2011). "A numerical study of microscale flow behavior in tight gas and shale gas reservoir systems." Transport in porous media **90**(1): 253.

Ghanbari, E. and H. Dehghanpour (2015). "Impact of rock fabric on water imbibition and salt diffusion in gas shales." International Journal of Coal Geology **138**: 55-67.

Hao, Y. B., et al. (2011). "Predominance of precipitation and temperature controls on ecosystem CO 2 exchange in Zoige alpine wetlands of Southwest China." Wetlands **31**(2): 413-422.

Higashi, K., et al. (1963). "Surface diffusion phenomena in gaseous diffusion. I. Surface diffusion of pure gas." Nippon Genshiryoku Gakkaishi (Japan) **5**.

Hornyak, G. L., et al. (2008). Introduction to nanoscience, CRC press.

Javadpour, F., et al. (2007). "Nanoscale gas flow in shale gas sediments." Journal of Canadian Petroleum Technology **46**(10).

Karniadakis, G., et al. (2006). Microflows and nanoflows: fundamentals and simulation, Springer Science & Business Media.

Kerr, R. A. (2010). Natural gas from shale bursts onto the scene, American Association for the Advancement of Science.

Kim, T. H., et al. (2017). "Evaluation of CO2 injection in shale gas reservoirs with multi-component transport and geomechanical effects." Applied energy **190**: 1195-1206.

Kuila, U. and M. Prasad (2011). Understanding pore-structure and permeability in shales. SPE Annual Technical Conference and Exhibition, Society of Petroleum Engineers.

Lan, Y., et al. (2017). "Pore compressibility of shale formations." SPE journal **22**(06): 1,778-771,789.

Langmuir, I. (1916). "The constitution and fundamental properties of solids and liquids. Part I. Solids." Journal of the American chemical society **38**(11): 2221-2295.

Loeb, L. B. (2004). The kinetic theory of gases, Courier Corporation.

Loh, H.-P. and N. Loh (2016). Hydraulic fracturing and shale gas: Environmental and health impacts. Advances in water resources management, Springer**:** 293-337.

Moridis, G. J., et al. (2010). Analysis of mechanisms of flow in fractured tight-gas and shale-gas reservoirs. SPE Latin American and Caribbean Petroleum Engineering Conference, Society of Petroleum Engineers.

Newsham, K. and J. Rushing (2001). An integrated work-flow model to characterize unconventional gas resources: Part I-Geological Assessment and Petrophysical Evaluation. SPE Annual Technical Conference and Exhibition, Society of Petroleum Engineers.

Rivard, C., et al. (2014). "An overview of Canadian shale gas production and environmental concerns." International Journal of Coal Geology **126**: 64-76.

Ross, D. J. and R. M. Bustin (2009). "The importance of shale composition and pore structure upon gas storage potential of shale gas reservoirs." Marine and petroleum Geology **26**(6): 916-927.

Shen, W., et al. (2017). "Gas flow behavior of nanoscale pores in shale gas reservoirs." Energies **10**(6): 751.

Shen, W., et al. (2016). "Numerical simulation of gas and water flow mechanism in hydraulically fractured shale gas reservoirs." Journal of Natural Gas Science and Engineering **35**: 726-735.

Sheng, G., et al. (2018). "Effect of microscale compressibility on apparent porosity and permeability in shale gas reservoirs." International Journal of Heat and Mass Transfer **120**: 56-65.

Strapoc, D., et al. (2010). "Geochemical constraints on the origin and volume of gas in the New Albany Shale (Devonian–Mississippian), eastern Illinois Basin." AAPG bulletin **94**(11): 1713-1740.

TinkerCad (2020). Autodesk tinkercad. https://www.tinkercad.com/dashboard.

Weijermars, R. (2013). "Economic appraisal of shale gas plays in Continental Europe." Applied energy **106**: 100-115.

Yu, W., et al. (2016). "Modeling gas adsorption in Marcellus shale with Langmuir and bet isotherms." SPE journal **21**(02): 589-600.

Yuan, J.-L., et al. (2013). "Borehole stability analysis of horizontal drilling in shale gas reservoirs." Rock Mechanics and Rock Engineering **46**(5): 1157-1164.

Yuan, Y. and S. Rahman (2016). "Extended application of lattice Boltzmann method to rarefied gas flow in micro-channels." Physica A: Statistical Mechanics and its Applications **463**: 25-36.

Zarragoicoechea, G. J. and V. A. Kuz (2004). "Critical shift of a confined fluid in a nanopore." Fluid phase equilibria **220**(1): 7-9.

Ziarani, A. S. and R. Aguilera (2012). "Knudsen's permeability correction for tight porous media." Transport in porous media **91**(1): 239-260.

Appendix

A. Derivation of N-dimensional sphere volume

For derivation of N-dimensional sphere volume we use the exact same procedure as finding the area under the Gaussian curve ($y = e^{-x^2}$).

First consider we want to calculate the area under the Gaussian:

$$\int_{-\infty}^{\infty} e^{-x^2} d_x = ? \tag{1}$$

For finding the answer of this integral we square the original expression and will find the answer:

$$(\int_{-\infty}^{\infty} e^{-x^2} d_x)^2 = \left(\int_{-\infty}^{\infty} e^{-x_1^2}\, d_{x_1}\right)\left(\int_{-\infty}^{\infty} e^{-x_2^2}\, d_{x_2}\right) = \int_{-\infty}^{\infty}\int_{-\infty}^{\infty} e^{-(x_1^2+x_2^2)}\, d_{x_1} d_{x_2} \tag{2}$$

Solving the latter integral is much easier now with the use of polar coordinates:

$$x_1 = r\sin\theta \tag{3}$$
$$x_2 = r\cos\theta \tag{4}$$
$$x_1 + x_2 = r^2 \tag{5}$$
$$d_{x_1} d_{x_2} = r d_r d_\theta = r d_r d_{\Omega_1} \tag{6}$$

It is worth to mention that when we are integrating over Ω_1 we are integrating along the unit circle, this will give us the perimeter of the unit circle or as so called "surface area of a 2-sphere".

Then we have:

$$\begin{aligned}\int_{-\infty}^{\infty}\int_{-\infty}^{\infty} e^{-(x_1^2+x_2^2)}\, d_{x_1} d_{x_2} = \int_{-\infty}^{\infty}\int_{-\infty}^{\infty} e^{-(x_1^2+x_2^2)}\, d_{x_1} d_{x_2} = \int_{r=0}^{\infty}\int_{\theta=0}^{2\pi} e^{-r^2}\, r d_r d_\theta \\ = \int_{r^2=0}^{\infty}\int_{\theta=0}^{2\pi} e^{-r^2}\frac{1}{2} d_{r^2} d_\theta\end{aligned} \tag{7}$$

If we replace r^2 by u, we will have:

$$\int_{u=0}^{\infty}\int_{\theta=0}^{2\pi} e^{-u}\frac{1}{2} d_u d_\theta = \frac{1}{2}\int_{\theta=0}^{2\pi} d_\theta \int_{u=0}^{\infty} e^{-u} d_u = \frac{1}{2} 2\pi(-e^{-u})_0^{\infty} = \pi \tag{8}$$

And then the original integral will be equal to $\sqrt{\pi}$.

The fact that we went through 2-dimensions by multiplying the integral in the beginning helped us to solve the original integral. Now the same procedure can be done in to 3-dimentions or even n-dimensions.

Rerunning the same procedure in 3-dimentions will help us to solve the one in n-dimensions.

$$(\int_{-\infty}^{\infty} e^{-x^2} d_x)^3 \tag{9}$$

In this solution instead of going to polar coordinates we can go to spherical coordinates

$$x_1 + x_2 + x_3 = r^2 \tag{10}$$
$$d_{x_1} d_{x_2} d_{x_3} = r^2 \sin\theta \, d_r d_\theta d_\varphi = r^2 d_r d_{\Omega_2} \tag{11}$$

As we mentioned in 2-dimensional case, integrating over Ω_2 is the same concept except for one dimension higher. As a result we are integrating over small patches of a surface of an sphere or "surface area of a 3-sphere".

If we take the same solution procedure the final answer for the above integral as expected will be:

$$(\int_{-\infty}^{\infty} e^{-x^2} d_x)^3 = (\sqrt{\pi})^3 \tag{12}$$

Now that we did the integral solution for the case 2 and 3 dimensions, we are going to solve it for n-dimensions:

$$\begin{aligned}(\int_{-\infty}^{\infty} e^{-x^2} d_x)^n &= \left(\int_{-\infty}^{\infty} e^{-x_1^2} \, d_{x_1}\right) \dots \left(\int_{-\infty}^{\infty} e^{-x_n^2} \, d_{x_n}\right) \\ &= \int_{-\infty}^{\infty} \dots \int_{-\infty}^{\infty} e^{-(x_1^2 + \dots + x_n^2)} \, d_{x_1} \dots d_{x_n}\end{aligned} \tag{13}$$

In this case we go to n-dimensional hyper spherical coordinates:

$$x_1 + \dots + x_n = r^2 \tag{14}$$
$$d_{x_1} \dots d_{x_2} = r^{n-1} d_r d_{\Omega_{n-1}} \tag{15}$$

By substituting the new coordinates we get:

$$\int_{-\infty}^{\infty} \dots \int_{-\infty}^{\infty} e^{-(x_1^2 + \dots + x_n^2)} \, d_{x_1} \dots d_{x_n} = \int e^{-r^2} r^{n-1} d_r \int d_{\Omega_{n-1}} \tag{16}$$

Similar to 2and 3 dimension, the angular part of the above integral will give us the "surface area of an n-sphere" or S_n. The radial part of the integral will be solved as follow:

$$\int e^{-r^2} r^{n-1} d_r = \int e^{-r^2} r^{n-2} \frac{1}{2} 2r \, d_r = \frac{1}{2} \int e^{-u} r^{\frac{n}{2}-1} d_u \tag{17}$$

The latter integral will give us the definition of Gamma function:

$$\frac{1}{2} \Gamma\left(\frac{n}{2}\right) = \frac{1}{2} \int e^{-u} r^{\frac{n}{2}-1} d_u \tag{18}$$

So the final solution will be:

$$(\int_{-\infty}^{\infty} e^{-x^2} d_x)^n = \frac{1}{2} \Gamma\left(\frac{n}{2}\right) S_n \tag{19}$$

Also we know that

$$(\int_{-\infty}^{\infty} e^{-x^2} d_x)^n = (\sqrt{\pi})^n \tag{20}$$

So we have:

$$S_n = \frac{\pi^{\frac{n}{2}}}{\frac{1}{2}\Gamma\left(\frac{n}{2}\right)} \tag{21}$$

This is the surface area of an n-sphere, and now we can simply calculate the volume of an n-sphere:

$$V(r) = \int S_n(r) d_r = \int S_n(r).r^{n-1} d_r = S_n \frac{r^n}{n} \tag{22}$$

Then if we consider a unit sphere ($r = 1$), we have:

$$V = \frac{S_n}{n} = \frac{\pi^{\frac{n}{2}}}{\frac{n}{2}\Gamma\left(\frac{n}{2}\right)} = \frac{\pi^{\frac{n}{2}}}{\Gamma\left(\frac{n}{2}+1\right)} \tag{23}$$

This will give us the volume of an n-sphere using Gamma function.

B. Stability Examination

If we consider the 1D simplified version of mas conservation equation

$$\frac{\partial p}{\partial t} = \frac{\partial^2 p}{\partial x^2} \tag{24}$$

If P_i^n be the solution of the equation for a forward difference scheme and the error $P_i^n + \varepsilon_i^n$ satisfy the same scheme

$$\frac{(P_i^{n+1} + \varepsilon_i^{n+1}) - (P_i^n + \varepsilon_i^n)}{\Delta t} = \frac{(P_{i+1}^n + \varepsilon_{i+1}^n) - 2(P_i^n + \varepsilon_i^n) + (P_{i-1}^n + \varepsilon_{i-1}^n)}{\Delta x^2} \tag{2}$$

As we know from the definition of P_i^n we can write

$$\frac{\varepsilon_i^{n+1} - \varepsilon_i^n}{\Delta t} = \frac{\varepsilon_{i+1}^n - 2\varepsilon_i^n + \varepsilon_{i-1}^n}{\Delta x^2} \tag{3}$$

We expand the error in a Fourier series and we have

$$\varepsilon_i^n = \sum_k \bar{\gamma}_k^n \exp(ikx_i) \tag{4}$$

Where $i = \sqrt{-1}$ and γ is the amplification factor

If we only consider one term in equation 4 (assuming that the solution has only one term), we get

$$\varepsilon_i^n = \bar{\gamma}^{\mathrm{n}} \exp(ikx_i) \tag{5}$$

We substitute 5 into 3 and solve for the amplification factor. The von Neumann criterion for stability is that the modulus of this factor must not be no greater than 1.

$$\frac{\bar{\gamma}^{\mathrm{n}+1} - \bar{\gamma}^{\mathrm{n}}}{\Delta t} = \frac{\bar{\gamma}^{\mathrm{n}} \exp(ikh) - 2\bar{\gamma}^{\mathrm{n}} + \bar{\gamma}^{\mathrm{n}} \exp(-ikh)}{h^2} \tag{6}$$

Since

$$\exp(ikh) - 2 + \exp(-ikh) = 2\cos(kh) - 2 = -4\sin^2(\frac{kh}{2}) \tag{7}$$

From equation 6 we get

$$\bar{\gamma}^{\mathrm{n}+1} = (1 - \frac{4\Delta t}{h^2}\sin^2(\frac{kh}{2}))\bar{\gamma}^{\mathrm{n}} \tag{8}$$

Dividing the equation by $\bar{\gamma}^{\mathrm{n}}$ gives

$$\bar{\gamma} = 1 - \frac{4\Delta t}{h^2}\sin^2(\frac{kh}{2}) \tag{9}$$

The von Neumann criterion for stability is satisfied if

$$|1 - \frac{4\Delta t}{h^2}\sin^2\left(\frac{kh}{2}\right)| \leq 1 \tag{10}$$

Thus, equation 10 is satisfied when the following stability condition holds.

$$\frac{\Delta t}{h^2} \leq \frac{1}{2} \tag{11}$$

We can perform a similar stability analysis for the backward difference scheme, in this case, the error equation takes the form

$$\frac{\varepsilon_i^{n+1} - \varepsilon_i^n}{\Delta t} = \frac{\varepsilon_{i+1}^{n+1} - 2\varepsilon_i^{n+1} + \varepsilon_{i-1}^{n+1}}{\Delta x^2} \tag{12}$$

After using the similar procedure as in forward difference scheme we will get the following equation for amplification factor

$$\bar{\gamma} = \frac{1}{1 + \frac{4\Delta t}{h^2}\sin^2(\frac{kh}{2})} \tag{13}$$

Which is always less than or equal to 1. Hence the backward difference scheme is unconditionally stable.

C. Role of "nstep" (Number of Steps) in the Dynamic Simulation

It is crucial to choose a suitable number of calculation steps to ensure we achieve (a) firm profiles and (b) accurate solutions. The splitting time step defines how often we switch between the solvers in our MATLAB solution to obtain the updated values. The number of steps defines the number of steps before the calculated solutions are shown.

We performed the entire solution using different values for the "nstep" to ensure all solutions converge to the same answer, and if the solver works correctly. The results of this simulations are shown in **Figure 33**.

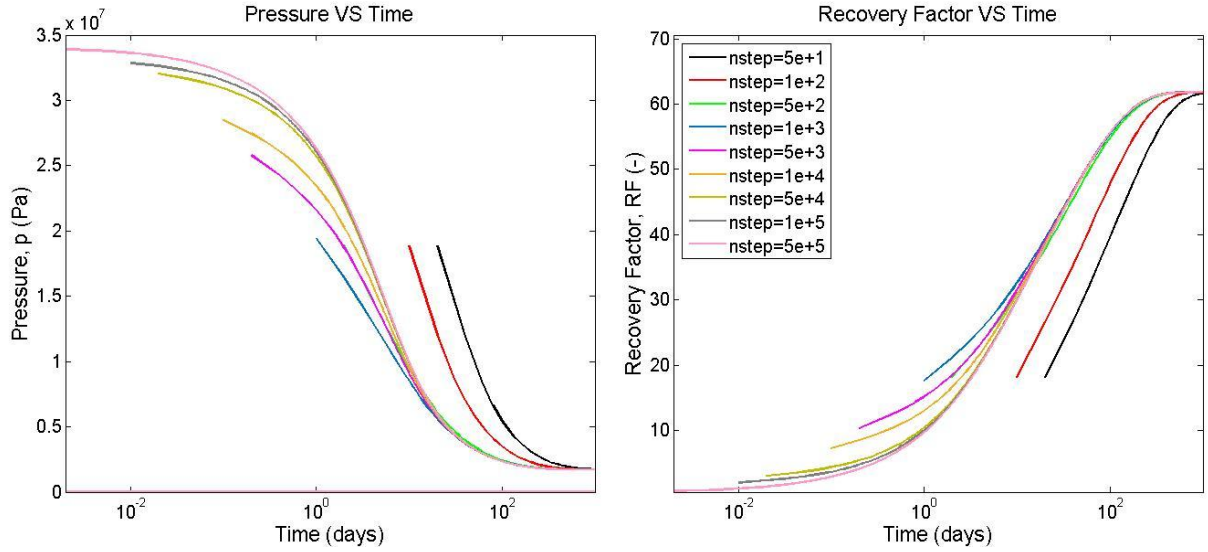

Figure 33 The effect of number of steps (nstep) on reservoir performance plots. Left Side: Reservoir pressure (Average pressure alongside the core) VS time (p vs T_{total}), Right Side: Recovery Factor VS time (RF vs T_{total}).

Figure 33 demonstrate the importance of choosing a suitable number of steps to obtain a stable and accurate solution. As we can see, all pressure plots and recovery plots converge to the same solution, which means the dynamic model works perfectly and it is stable for different values of "nstep".

It is also vital to mention that the value of "nstep" can directly affect our reservoir performance plots' accuracy. The total time of simulation is divided by the number of steps. The result defines the length of each time step on the x-axis of the plots. As we can see from the recovery plots on the right side of **Figure 33**, the bigger we choose the "nstep" value, the more accurate we obtain the first recovery factor value. For instance, if we choose $5e+5$ number of steps, the first recovery factor solution (0.7%) is obtained at time ($t = 0.002$ days) which is more realistic compare to the case when we choose $nstep = 5e+3$, in this case our first recovery factor solution is obtained at time ($t = 0.2$ days) and we can see that the value (10.4%) is less logical.

Even though it is more accurate to obtain high values of "nstep" for our dynamic model simulation, this will lead to a significantly time consuming simulation for each run. Therefore the optimized value of ($nstep = 1.5e+4$) was chosen for our dynamic simulation.